1 Introduction

Electron-atom collisions are responsible for a wide range of phenomena including plasma interactions, processes that occur in gas lasers and also interactions within the upper atmosphere, to name but a few. By studying electron-atom collisions we can therefore hope to better understand these processes. This introductory chapter is intended to review some of the previous experimental and theoretical work which were undertaken to achieve that goal. However, as all this work has already been reviewed extensively in the literature, only a précis will be given here.

A neutral atom, in the most general sense, consists of a small, heavy nucleus which is positively charged and one or more negatively-charged electrons orbiting this nucleus. A free electron colliding with this atom will experience a Coulomb force due to the atomic electron(s). While the nature of the Coulomb interaction is well known, the equations of motion, for even the simplest case of an electron scattering from a hydrogen atom, cannot be solved analytically due to the infinite range over which the interaction occurs. Thus we can consider electron-atom scattering theory to be characterised into two main problems (Burke *et. al.* 1971): defining the wavefunction of the target; and modeling the Coulomb interaction between the projectile electron and the target. Early studies of electron-hydrogen collisions, many of which have been reviewed by Burke and Smith (1962), provided the initial test-bed for theory and experiment. This is due to the fact that, in the case of atomic hydrogen, the target wavefunction is known exactly and this enables a clear focus on the electron scattering interaction. Despite this obvious theoretical advantage, atomic hydrogen has long been an experimentally challenging scattering target due to the

necessary dissociation of the hydrogen molecule into its atomic constituents (Dixon *et. al*. 1978). It is not surprising then that this work was soon extended to the more experimentally favourable “hydrogen-like” target sodium (Hertel and Stoll, 1974), which can be accurately modeled with a single electron orbiting an “inert” Hartree-Fock core. More recently, it has been shown that Convergent Close Coupling (CCC) calculations for electron scattering from sodium (Scholten *et. al.* 1993, Bray *et. al.* 1994), lithium (Karaganov *et. al.* 1999), potassium (Stockman *et. al.* 2001) and, to a lesser extent, rubidium (Hall *et. al.* 2004) are very successful in describing these respective scattering processes. This observation brings us to the question of whether heavier targets can be modeled using a similar approach, or whether relativistic effects must be included in an accurate theoretical description. Zeman *et. al.* (1995) have suggested that relativistic effects should be included in both the target description and the scattering process in order for the theoretical predictions to be correct, however no precise experimental data for such a system was available at that time.

The ultimate goal of any scattering experiment, in a general sense, is to determine the quantum states and the energy and momentum vectors of the interacting particles, before and after the collision (Bederson 1969a). If the energy, momentum and the complete set of quantum states is known for all particles, then all of the information for the system can be extracted by the experimentalist. However, in practice a typical scattering experiment will average over one or more of these parameters and some information is thus lost. Therefore, for an experiment to be a sensitive test of scattering theory, it is important that it can yield as many unique and independent parameters as possible. In order to describe both the magnitude and

relative phase of the scattering amplitudes, early experiments (see, for example, Eminyan *et. al.* 1973, Riley *et. al.* 1985) performed an analysis of the fluorescence radiation after the collision, using so-called electron-photon coincidence techniques (see also Andersen *et. al.* 1988). A further improvement came along with the development of narrowband tuneable-wavelength lasers that enable the scattering target to be prepared in a well defined excited state, from which the electron is superelastically scattered (Andersen *et. al.* 1988). While the amount of information extracted is essentially the same as for the early coincidence experiments, the superelastic technique resulted in much higher scattering count rates and therefore better precision (MacGillivray and Standage, 1991).

Previous inelastic electron scattering experiments with caesium had been limited to measurements of integral and total collision cross section data (Chen and Gallagher, 1978, MacAskill *et. al.* 2002). While angle-differential cross sections had been measured for other alkalis (see, for example, Hertel and Stoll, 1974), this was not the case for caesium until recently in the spin-resolved experiments of Baum *et. al.* (2004). Interestingly, the recent absolute total cross section data reported by Lukomski *et. al.* (2005) showed some considerable disagreement between experiment and current theoretical calculations at low to intermediate energies. In particular, they found significant disagreement at the 10eV electron energy, which is the same energy that the preliminary superelastic experiments (Karaganov *et. al.* 2001) were performed immediately prior to this study. Those measurements were later confirmed during the present project, and the results are presented in chapter 6 of this thesis. To date, comprehensive and complete sets of experimental data for superelastic electron scattering from caesium have not been available. Hence, one of

the aims of the work outlined in this thesis is to provide a complete set of spin-averaged parameters for superelastic electron scattering from the $6^2P_{3/2}$ excited state of caesium. In doing so the leading modern theories developed and refined in recent times can be tested alongside this experimental data. The expectation is that the current data will contribute to addressing the questions on the role of relativistic effects in electron-atom collisions and, more generally, to be a useful aid in the development of the theory.

In addition to the experimental work reported in this thesis, a review of some of the common framework employed in any literature is detailed in chapter 2. This chapter also contains a brief discussion of the various theoretical approaches to predicting the scattering amplitudes for electron-atom collisions. Specifically a relativistic distorted wave method, the convergent close-coupling method and the R-matrix approach are described. Finally some relevant experimental approaches are discussed, with particular focus on the superelastic technique. The current experimental apparatus is presented in detail in chapter 3, from the initial design to any modifications made to the major components during my experimental studies and to some practical notes regarding working with caesium. A new laser frequency stabilisation technique has been adopted for the current experimental study, which is considered to be a key improvement on previous arrangements. While modification of the existing apparatus to produce a beam of caesium atoms was relatively straightforward, it was noticed in previous work in the Flinders group that the technique for stabilising the laser frequency, by using a split photodiode and the Doppler effect, was itself potentially unstable. This was due to the fact that the fluorescence intensity from the interaction region depended on the polarisation of

the laser, which was changed during the course of an experimental run. The solution to this problem was to stabilise the laser frequency before the laser entered the interaction region, using a saturated absorption spectroscopy technique. This approach was successful in maintaining the laser frequency locked to the desired transition frequency to within a few MHz for as long as 20 hours without failure. Further detailed discussion of this arrangement can be found in chapter 3. The optical pumping method employed to prepare the caesium atoms into a well defined excited state for each of the measured parameters is discussed in chapter 4. This chapter also includes some successful theoretical models which have been employed for other alkali-metal targets and a review of previous relevant studies into optical pumping. Experimental procedures employed throughout the present project are reported in chapter 5, including details of several significant sources of potential systematic error which have been addressed. A complete analysis of the systematic and statistical errors relevant to the data of the present experiments is also given here. Finally, the technique which was utilised to account for the instrumental angular resolution and finite interaction volume effects is discussed in chapter 5. The results measured as a part of this study are presented in chapter 6, both in graphical form, alongside the predictions of a number of modern theoretical approaches, and in numerical form at the end of the chapter. Conclusions from this work are drawn in chapter 7.

2 Electron-Atom Collisions

2.0 Introduction

During an electron-atom collision any of a number of processes can occur. For example, if the energy of the incoming electron is high enough, it may lose some of its energy during the interaction resulting in a bound electron from the atom being ejected and the atom is said to be ionised. In another scenario, the atom may emerge from the collision with no excitation and accordingly the scattered electron energy remains essentially unchanged. This type of collision is referred to as an elastic collision. Another important process, which is the time reversed equivalent of that which we are concerned with for the present study, is the inelastic collision. Here the incoming electron excites a bound electron of the atom to a higher eigenstate, and the scattered electron energy is the difference between its initial energy and the energy of excitation for the atomic eigenstate of interest. As an example relevant to the experiments reported in this thesis, consider the excitation of the first P-state of caesium. Here we have an incoming electron losing some of its energy to the atom, with the outer-most electron bound to that atom being excited from its $6^2S_{1/2}$ ground state to the $6^2P_{3/2}$ excited state. The excited atom now rapidly undergoes spontaneous decay back to its ground state, emitting a photon. The entire process is summarised by the following reaction equations:

$$e(E) + Cs(6^2S_{1/2}) \rightarrow e(E - 1.455eV) + Cs(6^2P_{3/2})$$

$$Cs(6^2P_{3/2}) \rightarrow Cs(6^2S_{1/2}) + \gamma(1.455eV) \qquad \text{(eq. 2.1)}$$

where E is the incident energy of the electron.

Due to its rich hyperfine structure, the S-P transition of caesium involves the excitation of many degenerate magnetic sublevels, and it is the relative populations of these sublevels that determine the shape of the excited atom and its angular momentum. In order to understand the scattering mechanism and describe the dynamics of the electron-atom interaction, we must have a unified framework within which the shape and angular momentum of the excited atom can be described. This chapter therefore aims to briefly outline this framework in the standard approach of Andersen *et. al.* (1988), with particular focus on the specific case of spin-averaged inelastic electron scattering from caesium.

2.1 The Density Matrix

Following Blum (1981), a coherently excited atom (i.e. an atom which has been completely prepared so that it is in a pure state), under certain conditions of symmetry, can be represented in quantum mechanics by a wavefunction which is a linear superposition of basis states ϕ_i (Macek and Hertel 1974):

$$|\psi\rangle = \sum_i a_i |\phi_i\rangle \qquad \text{(eq. 2.2)}$$

where the sum over *i* refers to a set of quantum numbers. In practice this complete preparation of a system rarely occurs and therefore it cannot be described by a single-state vector. Due to this lack of knowledge of the prepared system, the system must therefore be described as a mixture of states. Consider a system which has been incoherently excited, that is one which is a mixture of independently prepared states $|\psi_n\rangle$ (n=1,2,…), with statistical weights W_n. Such a system is conveniently described, in the $|\phi_i\rangle$ representation, by a density matrix ρ, where:

$$\rho_{ij} = \langle \phi_i | \rho | \phi_j \rangle = \sum_n W_n a_i^{(n)} a_j^{(n)*} \qquad \text{(eq. 2.3).}$$

This system has certain probabilities, $W_1, W_2, ..., W_i$, of being in the pure states $|\phi_1\rangle, |\phi_2\rangle, ..., |\phi_i\rangle$ (Blum 1981). The matrix elements of ρ are $\langle a_i^{(n)} a_j^{(n)*} \rangle$, and the so-called scattering amplitudes, a_i, contain all of the information on the scattering process. Clearly, in order to completely describe the scattering process, all of the density matrix elements for the excited state must be determined. The elements can be interpreted as follows: each diagonal element gives the population of the respective $6^2P_{3/2}$ substates. The off-diagonal elements correspond to coherences formed between the various substates.

One well-known experimental approach to gaining limited information about the collision system is to measure the scattering intensity from the atom, i.e. the differential cross section (DCS), as a function of the scattering angle. Each diagonal element of the density matrix can be considered as the partial DCS for the corresponding magnetic sublevel:

$$\rho_{ii} = \langle |a_i|^2 \rangle = \sigma(i) \qquad \text{(eq. 2.4)}$$

where $\sigma(i)$ is the partial DCS for the i^{th} sublevel. Therefore, one can write the total DCS for the system as the sum of the diagonal elements of ρ:

$$\sigma = \sum_i \sigma(i) = Tr\rho \qquad \text{(eq. 2.5).}$$

and it can be seen that σ gives some information pertaining to the magnitude of the scattering amplitudes, albeit averaged over the magnetic sublevels. The important physical information that is not provided by σ is the phase of the each of the scattering amplitudes a_i, which is contained in the complex off-diagonal elements of the density matrix ρ. It is highly desirable to measure these elements of the density

matrix, as they give a complete description of the collision process at a fundamental level. This is possible, at least in principle, if an experiment is designed that can select each specific excitation separately so that averaging is avoided. Techniques of this type are generally referred to as alignment and orientation studies, following the early work of Macek and Jaecks (1971), Hertel and Stoll (1974) and the more recent reviews of Andersen *et. al.* (1988, 1995).

In order to describe the alignment and orientation of the P-state, a suitable reference frame must first be chosen. The symmetry of the collision system suggests that the frame be chosen so that it includes the scattering plane, defined by the incident and scattered electron momentum vectors $\vec{k}_{in}$ and $\vec{k}_{out}$. Three possible choices of reference frames are illustrated in figure 2.1. The atomic frame has its x^a-axis given by the symmetry axis of the P-state charge cloud, which is also a symmetry axis for the radiation pattern. The natural and collision frames have their x^n and z^c coordinate axes parallel to the incident electron momentum $\vec{k}_{in}$, while the z^n and y^c axes are parallel to the direction of momentum transfer.

Following Blum (1981), we consider the particular case where the spins of both the electron and atom are not known either before or after the collision (i.e. the spin states are averaged during measurement). The 6^2P state of caesium can be described, in the collision frame, as a mixture of states:

$$\left|6^2P\right\rangle^{(s)} = a_0^{(s)}\left|\ 0\right\rangle + a_1^{(s)}\left(\left|+1\right\rangle - \left|-1\right\rangle\right) \qquad \text{(eq. 2.6a)}$$

$$\left|6^2P\right\rangle^{(t)} = a_0^{(t)}\left|\ 0\right\rangle + a_1^{(t)}\left(\left|+1\right\rangle - \left|-1\right\rangle\right) \qquad \text{(eq. 2.6b)}$$

where the superscripts (s) and (t) denote singlet and triplet excitation with probabilities of $W^{(s)} = 1/4$ and $W^{(t)} = 3/4$ respectively. In this case, the density matrix is:

$$\rho = \begin{pmatrix} \left\langle \left| a_{+1} \right|^2 \right\rangle & \left\langle a_{+1} a_0^* \right\rangle & \left\langle a_{+1} a_{-1}^* \right\rangle \\ \left\langle a_{+1} a_0^* \right\rangle^* & \left\langle \left| a_0 \right|^2 \right\rangle & \left\langle a_0 a_{-1}^* \right\rangle \\ \left\langle a_{+1} a_{-1}^* \right\rangle^* & \left\langle a_0 a_{-1}^* \right\rangle^* & \left\langle \left| a_{-1} \right|^2 \right\rangle \end{pmatrix} \qquad \text{(eq. 2.7)}$$

and the elements,

$$\begin{aligned} \rho_{ii'} &= \left\langle a_i a_{i'}^* \right\rangle = \sum_i W^{(n)} a_i^{(n)} a_{i'}^{(n)*} \\ &= \frac{3}{4} a_i^{(t)} a_{i'}^{(t)*} + \frac{1}{4} a_i^{(s)} a_{i'}^{(s)*} \end{aligned} \qquad \text{(eq. 2.8),}$$

are an average over the singlet and triplet states. If we can assume reflection symmetry of the P-state, the 9 matrix elements reduce to 3 independent parameters, with several choices being available for these parameters (Andersen *et. al.* 1988). One such choice is the set of alignment and orientation parameters $L_\perp$, $\overline{P}_L$ and γ. In the natural frame they are calculated in terms of the density matrix elements as follows:

$$\begin{aligned} L_\perp &= \rho_{11}^{nat} - \rho_{-1-1}^{nat} \\ \overline{P}_L &= 2\left|\rho_{-1-1}^{nat}\right| \\ \gamma &= -\frac{1}{2}\arg\left(\rho_{-1-1}^{nat} \pm \frac{\pi}{2}\right) \end{aligned} \qquad \text{(eqs. 2.9).}$$

These three parameters have the advantage that they enable the post-collisional electron charge cloud to be visualised in terms of alignment and orientation (see figure 2.2). In this characterisation, $L_\perp$ describes the angular momentum transferred

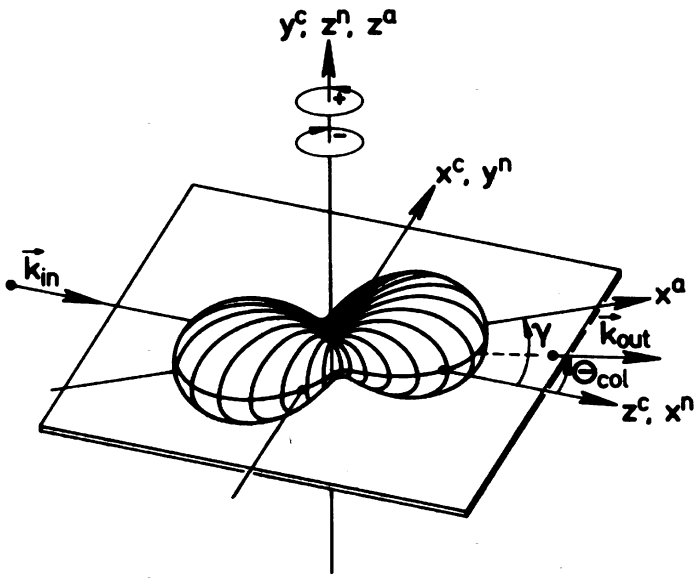

Figure 2.1: Three possible choices of reference frames for describing the post-collision P-state. The superscript c *denotes the standard collision frame,* n *denotes the natural frame and* a *denotes the atomic frame. Each frame transforms into the other on rotation (figure is from Andersen et. al. 1985).*

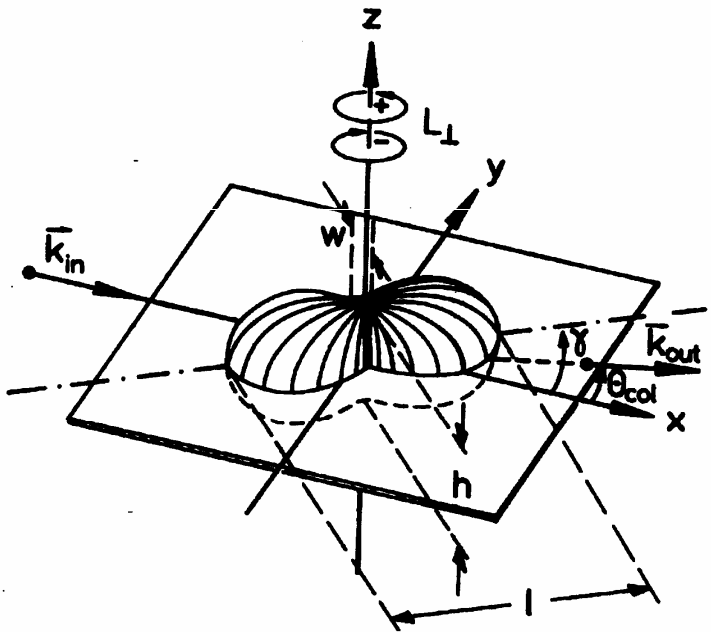

Figure 2.2: Parameterisation of the P-state electron charge cloud in the natural frame. The P-state is described in terms of the angular momentum transferred perpendicular to the scattering plane ($L_\perp$), the alignment angle (γ) and the relative length (l), width (w) and height (h) of the electron charge cloud (figure is from Andersen et. al. 1988).

perpendicular to the scattering plane, γ is the alignment angle after collision and $\overline{P}_L$ is the linear polarisation, given by:

$$\overline{P}_L = \frac{l - w}{l + w} \qquad \text{(eq. 2.10)}$$

where l and w are the length and width of the post-collisional electron charge cloud, respectively. Experimental data is usually measured directly in terms of the Stokes vector components P_1, P_2 and P_3, a notation which has been borrowed from the same terminology used in the description of polarised light (Shurcliff 1966). These three parameters can be measured directly and derive from measurements of the scattering rate in coincidence with a given polarisation of decay fluorescence:

$$P_1 = \frac{I(0^\circ) - I(90^\circ)}{I(0^\circ) + I(90^\circ)} \qquad \text{(eq. 2.11a)}$$

$$P_2 = \frac{I(45^\circ) - I(135^\circ)}{I(45^\circ) + I(135^\circ)} \qquad \text{(eq. 2.11b)}$$

$$P_3 = \frac{I(RHC) - I(LHC)}{I(RHC) + I(LHC)} \qquad \text{(eq. 2.11c)}$$

where $I(\theta^\circ)$ denotes the number of coincidence events with the fluorescence polarised in the θ direction, while $I(RHC)$ and $I(LHC)$ are the number of events for right-hand and left-hand polarised fluorescence, respectively. The Stokes parameters can be related to the alignment and orientation parameters by the following:

$$\begin{aligned} L_\perp &= -\overline{P}_3 \\ \overline{P}_L &= \sqrt{\overline{P}_1 + \overline{P}_2} \\ \gamma &= \arg(\overline{P}_1 + i\overline{P}_2) \end{aligned} \qquad \text{(eq. 2.12).}$$

Here $\overline{P}_i$ refer to the measured Stokes parameters after corrections for hyperfine structure effects (MacGillivray and Standage 1991). These corrected Stokes parameters are generally known as the *reduced* Stokes parameters, so as to distinguish them from the parameters of equations 2.11.

2.2 Theoretical Approaches

The electron-caesium collision problem has received considerable interest for many years as a test-bed for describing the interaction between an electron and a heavy target atom. It has provided several challenges in approaching a complete theoretical description, particularly in the low to intermediate energy regime that is the concern of the present experimental study. Early calculations emphasised the importance of using a relativistic approach while truncating the full set of target states in order to enable numerical solutions (Burke and Mitchell 1974, Walker 1974, Karule 1972). While there was no experimental data for electron-caesium scattering at the time, these theoretical predictions suggested that relativistic effects were observable. This theoretical work, and indeed most current theoretical work, can be grouped into the two broad categories of either distorted wave methods or close-coupling methods. The distorted wave approach is a first-order (or in some cases higher order) improvement on the Born approximation, which assumes that the interaction between the electron and the neutral target is weak (Sobel'man 1972). The first improvement to the Born approximation, as made by the distorted wave method, is to include the distortion of the projectile electron wavefunction due to the target atom as a perturbation of the free-particle motion. By contrast, the close-coupling approach is a non-perturbative technique whereby the wavefunction for the scattering system as a whole is expanded in terms of a complete set of discrete and

continuum states. The description of the scattering process in this case depends upon the terms that are included in the expansion, so early close-coupling calculations were found to best describe low-energy collisions, where the target excitation was limited to the first few low-energy states. However if the appropriate terms are used in the expansion, particularly given the ever-increasing computing power available, the close-coupling approach can be extended to higher-energy collision systems (Andersen and Bartschat, 2001). There are two important assumptions that are common to each of the theories that will be discussed here. Firstly, the caesium atom is considered to consist of a single outer-shell electron orbiting outside an inert core, so that none of the 54 core electrons interact directly with the projectile, irrespective of the incident energy. Secondly, the scattering process is time-invariant, which enables us to treat the superelastic scattering process in much the same way as the inelastic process.

The first published results for the angle-dependent Stokes parameters for caesium were a relativistic distorted wave (RDW) calculation by Zeman *et. al.* (1993). The RDW method is a relativistic approach, solving the Dirac equation within the *jj*-coupling scheme, with the target modeled by a non-local potential (Zeman *et. al.* 1994, 1997). As the distorted wave approach assumes the interaction between the incident electron and the target is weak, it is perhaps not surprising that these calculations for alkali atoms have been found to generally reach better agreement with experimental results at forward angles and for higher incident electron energy (Karaganov *et. al.* 2002, Stockman *et. al.* 1999). Results of several distorted-wave calculations for electron-alkali atom collisions are reported in the review of Andersen *et. al.* (1997).

The convergent close coupling (CCC) theory, first introduced by Bray and Stelbovics (1992), approaches the electron-caesium scattering problem by attempting a complete description of the target discrete and continuum states through a finite basis set representation in a non-relativistic framework. The CCC first defines the target Hamiltonian, which contains terms for the kinetic and potential energy of the bound electron. In general, and particularly in the case of heavy atoms such as caesium, the term containing the core potential must be carefully approximated in treating the interaction between the projectile electron and the 54 core electrons as a whole. The CCC employs a Hartree-Fock frozen-core potential with the addition of a phenomenological core polarisation (Bray 1994):

$$V_1 = V^{FC} + V^{pol} \qquad \text{(eq. 2.13).}$$

Some examples of the techniques which can be applied to formulate the terms V^{FC} and V^{pol} are found in Bray (1994). The total Hamiltonian, H, for the entire projectile-target system can now be established by introducing similar terms for the projectile electron, along with the potential V_{01} describing the projectile-target electron interaction:

$$\begin{aligned} H &= K_1 + V_1 + K_0 + V_0 + V_{01} \\ &= K_1 + V_1^{FC} + V_1^{pol} + K_0 + V_0^{FC} + V_0^{pol} + V_{01} \end{aligned} \qquad \text{(eq. 2.14),}$$

where the bound and projectile electrons are distinguished by the subscripts 1 and 0, respectively. The time-independent Schrödinger equation for the system is:

$$\left(E - H\right)\left|\Psi\right\rangle = 0 \qquad \text{(eq. 2.15),}$$

where E is the total energy of the system and $\left|\Psi\right\rangle$ is the total wavefunction describing the motion of the projectile electron and the atomic charge cloud. For a

complete description of the system, $|\Psi\rangle$ should be expanded over the complete set of target states. In general, this expansion will be over an infinite number of bound and continuum states for an atomic target, which yields an infinite set of coupled-channel differential equations. In order to manage this problem computationally, the CCC expands the total wavefunction onto a finite basis set, whose eigenstates are called pseudostates. These pseudostates are chosen so that the entire set of target states is represented by a finite set of N square-integrable functions (Bray and Stelbovics 1995). Thus the problem is reduced to a finite set of coupled integral equations, providing numerical solutions for the scattering amplitudes of the system of interest. The numerical solutions are not exact, however they will converge to the desired accuracy with increasing basis size N.

The R-matrix approach to the electron-caesium problem is another close-coupling technique where relativistic effects can be included through the use of the Dirac equation (Burke and Mitchell 1974), or alternatively through the Breit-Pauli Hamiltonian (Scott and Burke 1980). These two approaches have been compared by Bartschat (1993). The R-matrix treatment divides the scattering problem into two well defined regions: the internal region, bound by a sphere of radius large enough to include the atomic target states and possible pseudostates of interest in the calculation; and the external region outside the sphere where the target potential is reduced to a weak long-range multipole potential (Burke and Scott 1996). The solution at the boundary between the two regions yields the matrix *R*, which leads to the scattering matrix *S*, whose elements are the scattering amplitudes for the problem. In the recent Breit-Pauli R-matrix with pseudostates (RMPS) method of Bartschat and Fang (2000) the target was modeled by a static core potential, along

with several additional terms accounting for spin-dependent potentials and relativistic corrections. The target structure and coupling between the discrete and continuum states was treated through an expansion onto a finite basis of 8 physical states and 32 pseudostates. The basis was chosen so that the pseudostate angular momenta range from below the ionisation threshold to well into the target continuum.

Numerical data for the reduced Stokes parameters for electron-caesium scattering, from recent CCC (Bray 2006) and RMPS (Bartschat 2006) calculations, have been kindly provided by Prof. Igor Bray and Prof. Klaus Bartschat. They are presented along with the experimental results of the current project in chapter 6.

2.3 Experimental Approaches

As Bederson (1969a, 1969b) first noted in his article, "The Perfect Scattering Experiment", the goal of such a scattering experiment is to determine all of the quantum numbers of the initial and final states of the colliding particles, along with the energy and momenta of the incident and scattered electrons. That is, with respect to the density matrix formalism, to determine the magnitude and phase of all of the scattering amplitudes. For the case of an inelastic collision experiment involving the ground state of caesium, this would equate to colliding a spin-polarised electron with the spin-polarised ground state Cs atom, and measuring the exact final state of the atom through analysis of the decay fluorescence, in coincidence with the detected scattered electron. The process can be illustrated by the equation:

$$Cs(\alpha) + e(\beta) \rightarrow Cs(\alpha') + e(\beta') \qquad \text{(eq. 2.16)}$$

where α, β, α' and β' describe the initial and final states of the electron and the atom and are known exactly, along with their initial and final momentum vectors. Anderson *et. al.* (1997) have shown that a complete determination of all of the parameters in Bederson's "perfect experiment" is a very complicated matter. Nevertheless there is still much to be learnt from spin averaged experiments which can measure the phase of the scattering amplitudes, particularly now that there are theories that can predict these amplitudes. This was not the case in 1969.

Consider now the time-reverse equivalent of the inelastic scattering experiment of equation 2.1:

$$Cs(6^2S_{1/2}) + \gamma(1.455eV) \rightarrow Cs(6^2P_{3/2})$$

$$e(E - 1.455eV) + Cs(6^2P_{3/2}) \rightarrow e(E) + Cs(6^2S_{1/2}) \qquad \text{(eq. 2.17).}$$

Here the atom is first prepared to the excited state of interest through optical pumping in a polarised laser field, before the electron-atom collision. When the electron is scattered from the excited atom, it collisionally de-excites the atom, gaining energy equal to the energy of excitation. Hence electron-atom collisions of this type are generally referred to as being "superelastic". Advances in tunable continuous-wave (CW) lasers, beginning in the 1970's, and in particular most recently with diode lasers, have enabled superelastic studies of a wide range of atomic systems, including electron interactions with sodium (Scholten *et. al.* 1993), lithium (Karaganov *et. al.* 1999), potassium (Stockman *et. al.* 2001), rubidium (Hall *et. al.* 2004), calcium (Law and Teubner 1995, Murray and Cvejanovic 2003), helium (Jacka *et. al.*), chromium (Hanne *et. al.* 1993) and barium (Johnson and Zetner 2005).

The superelastic experiment provides exactly the same information as the inelastic coincidence experiment, under the assumption that the scattering mechanism of interest is invariant on time reversal (Andersen *et. al.* 1988). There are, however, several technical advantages to the superelastic approach (MacGillivray and Standage 1991). One such advantage is that discrimination between the superelastic signal and the lower energy elastic background is straightforward, using a retarding field-type electron spectrometer. Additionally, as the diameter of the interaction region is controlled by the laser beam (see section 3.2.5), it can be easily confined or expanded from outside the scattering chamber with the use of standard optical instruments and without the need for adjusting the atomic or electron beams. Finally, the number of accessible excited states of the atom is reduced to a single photon-induced transition, controlled by the frequency tuning of the laser, whose energy resolution is much better than that which can be achieved with an electron beam. In addition to this, the superelastic technique, unlike coincidence scattering, is not a time-resolved process and therefore has a much faster data collection rate. All of these conditions ultimately lead to the superelastic technique yielding a higher scattering signal than the equivalent coincidence measurements, for otherwise equal atomic and electron beam parameters, therefore enabling a broader range of energies and scattering angles to be studied.

Measurement of the number of superelastic electron scattering events as a function of laser polarisation, for a given scattering angle, yields the parameters:

$$P_1 = \frac{I(0^\circ) - I(90^\circ)}{I(0^\circ) + I(90^\circ)}$$
$$P_2 = \frac{I(45^\circ) - I(135^\circ)}{I(45^\circ) + I(135^\circ)} \qquad \text{(eq. 2.18)}$$
$$P_3 = \frac{I(RHC) - I(LHC)}{I(RHC) + I(LHC)}$$

where $I(\theta^\circ)$ is now the superelastic electron scattering rate for linear laser polarisation θ°, while $I(RHC)$ and $I(LHC)$ are the rates for the respective right-handed and left-handed laser polarisations. The parameters P_i do not correspond exactly to the components of the Stokes vector (equations 2.11) as optical pumping effects must be included (see chapter 4). Specifically, these effects are dealt with by the so-called optical pumping coefficients K and K', where:

$$\overline{P_1} = \frac{1}{K} P_1$$
$$\overline{P_2} = \frac{1}{K} P_2 \qquad \text{(eq. 2.19).}$$
$$\overline{P_3} = \frac{1}{K'} P_3$$

K and K' thereby enable depolarisation during the optical pumping process to be included in the collision characterisation. The reduced Stokes parameters in equation 2.19 are now identical to those of equation 2.12.

2.4 Coherence

Coherence can be characterised by the frame-independent parameter P^+, where:

$$P^+ = \sqrt{\overline{P_1}^2 + \overline{P_2}^2 + \overline{P_3}^2} \leq 1 \qquad \text{(eq. 2.20).}$$

It is related to the separate singlet and triplet scattering amplitudes by (Andersen *et. al.* 1988):

$$\left(P^{+}\right)^{2} = 1 - \frac{3}{4}\left| a_{1}^{(t)} a_{-1}^{(s)} + a_{-1}^{(t)} a_{1}^{(s)} \right|^{2} \qquad \text{(eq. 2.21).}$$

For a pure triplet or singlet channel, the P-state is completely spin polarised and $P^{+} = 1$. However, if there is no discrimination between the spin-dependent channels an incoherent mixture of spin states exists and the parameter P^{+} will reflect the phase relationship between the spin-averaged amplitudes a_{1} and a_{-1}. In general, for the spin-averaged experiment, P^{+} is positive and less than or equal to unity: $0 \le P^{+} \le 1$ (Andersen *et. al.* 1988).

Even without any knowledge of the individual spin states of the electron or the atom, it is possible to gain some information on the role of the spin-dependent processes. Consider the coherence parameter with triplet and singlet scattering amplitudes converted into direct (D) and exchange (E) scattering amplitudes (Kessler 1985):

$$\left(P^{+}\right)^{2} = 1 - 3\left| a_{1}^{D} a_{-1}^{E} - a_{-1}^{D} a_{1}^{E} \right|^{2} \qquad \text{(eq. 2.22)}$$

Equation 2.22 is only less than unity if the exchange scattering amplitudes, a_{i}^{E}, are non-zero. Thus some information about the role of exchange scattering can be extracted from the spin-averaged experiment (Teubner and Scholten 1992).

3 Apparatus

3.0 Introduction

This chapter describes the apparatus employed in the electron-caesium superelastic scattering experiments discussed in this thesis. The original apparatus was designed by Riley (1984) for the purpose of studying angular correlation functions in sodium. Subsequent modifications by Scholten (1989), Law (1995), Karaganov (1997) and Stockman (1998), have allowed experiments involving electron scattering from optically excited sodium, calcium, lithium and potassium targets, respectively, to be investigated. Some additional modifications were made during the course of the present study, in order to meet the demands of the electron-caesium scattering experiments, and these will be discussed in detail later in this chapter.

3.1 Scattering Chamber and Experimental Arrangement

3.1.1 Vacuum System

The scattering chamber consisted of a large (76cm dia. x 82cm height) stainless steel cylinder mounted on top of 2.5cm thick stainless steel base plate. It was pumped by an Edwards Diffstak MK2 Series 160/700P oil diffusion pump, backed by an Edwards EDM20 rotary mechanical pump. A refrigerated cold finger (-55^{o}C), positioned in the foreline before the rotary pump, prevents oil from the diffusion pump, or water vapour from the chamber roughing process, migrating into the backing system. A pneumatically actuated butterfly valve was in place between the scattering chamber and the diffusion pump. The entire apparatus was positioned on a wooden platform, and was opened by raising the bell with three hydraulic lifters stationed around the outer perimeter of the chamber. A schematic diagram of some

of the major components of the apparatus is shown in figure 3.1. The chamber pressure was monitored using a Granville-Phillips Series 274 ionisation gauge, while the backing pressure was monitored by a Granville-Phillips Pirani gauge. Typical chamber pressures were $1x10^{-7}$ Torr, when the caesium oven was cold, and $2.5x10^{-7}$ Torr with the oven at operating temperature.

3.1.2 Turntables

The electron gun and analyser could each be independently rotated in the scattering plane by twin turntables mounted on a 15mm thick brass platform, which was connected directly to the base of the scattering chamber. The turntables were positioned so that they were coaxial with the laser beam which was aligned to the centre of the chamber (see figure 3.2). Each turntable was constructed from brass and moved freely atop a race of phosphor bronze ball bearings. The scattering angle could be varied by rotating either turntable manually via helical gears. The angle was monitored by a potentiometer on each gear, yielding an estimated uncertainty of better than $\pm 0.2°$.

3.1.3 Electromagnetic Fields and Shielding

For any electron scattering study it is crucial that the experiments are performed in an environment free of unwanted electromagnetic fields. It was therefore essential that the apparatus was constructed exclusively from non-magnetic materials. The vacuum chamber walls were constructed from 310 stainless steel, which was selected due to its low magnetic permeability. The side of the chamber was also lined with conetic shielding and an outer mu-metal shield to reduce the presence of any ambient magnetic fields. Electrical feedthroughs and cables were all shielded

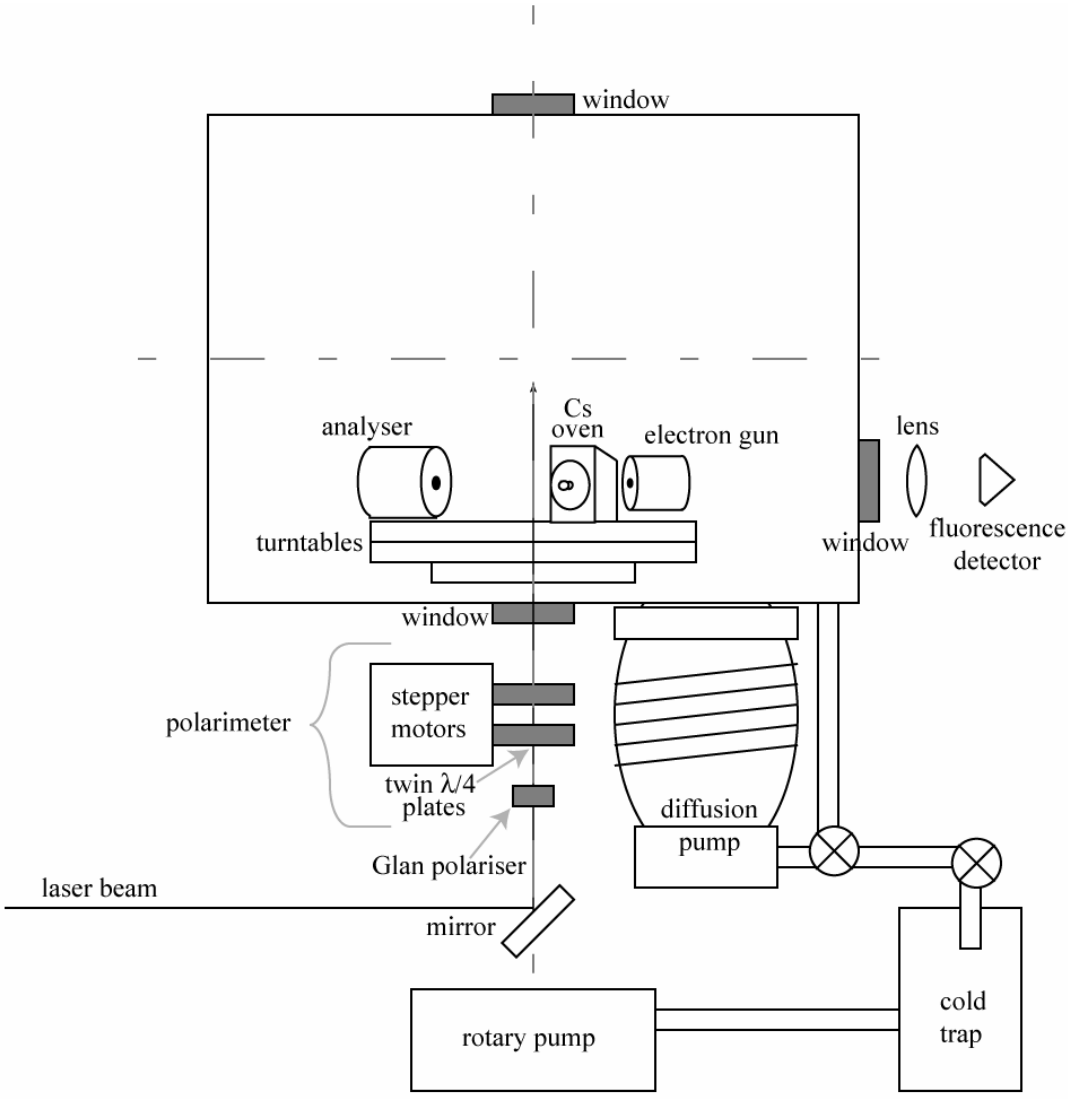

Figure 3.1: A schematic diagram of the vacuum apparatus and some of the major components used in the caesium experiments (not to scale).

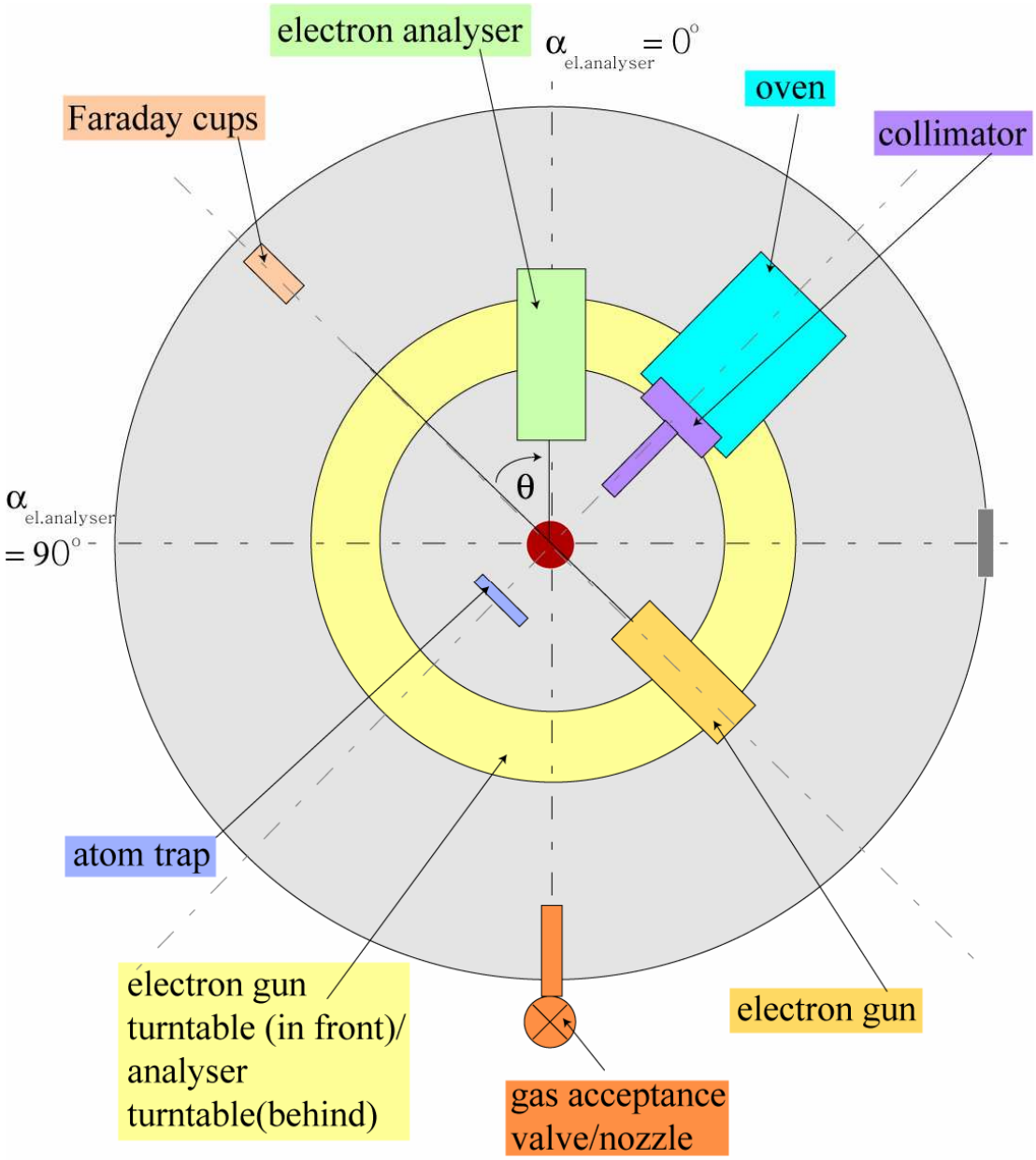

Figure 3.2: Schematic illustration of the experimental layout, as viewed from above (not to scale). The laser direction is out of the page.

and care was taken to ensure that all metal surfaces were maintained at ground potential. Orthogonal pairs of Helmholtz coils, one circular (1.8m diameter) pair and one square (2m x 2m) pair, were additionally set in place to further negate the vertical and North-South components of the ambient magnetic field respectively. These nett field components were measured, using a Schonstead Instrument Co. Model DM2220 magnetometer, to be less than 5mG in each case at the interaction region. The East-West magnetic field component was found to be negligible.

3.1.4 Cleaning

Throughout the experiments the entire vacuum system required regular cleaning due to the corrosive and extremely hydrophilic nature of caesium. Any residual traces of caesium would tend to combine with water molecules to produce caesium hydroxide, an undesirable product due to its dielectric and highly corrosive properties. While strategies were in place to minimise the possibility of unwanted residual caesium being introduced into the apparatus, it was ever important to perform regular and thorough cleaning of the scattering chamber in order to maintain good vacuum conditions and to prevent possible electrostatic charging effects. These latter effects could, for example, lead to a serious deterioration in the performance of the electron gun if left unaddressed.

3.2 Atomic Beam

3.2.1 Caesium Beam Source

Caesium, with 55 electrons, is the 5^{th} alkali metal in the periodic table. Its only naturally occurring isotope, ^{133}Cs, is known as the most electronegative stable metal and, along with rubidium and potassium, it is highly reactive. It is a soft metal with a

shiny, silvery gold colour. Other physical properties of caesium can be found in table 3.1.

Safe handling of alkali metals in the laboratory is imperative and in the case of caesium it is essential that the metal is not allowed to contact any surface, unless that surface has been specifically prepared for the task. Contact with air or water, as well as many material surfaces, will lead to rapid oxidation at best and explosive fire at

Atomic Number	55
Atomic Mass	132.91 u
Melting Point (STP)	28.40 ^{o}C
Boiling Point (STP)	678.4 ^{o}C
Specific Gravity (20^{o}C)	1.873 g cm^{-3}
Effective Atomic Diameter (Cs vapour)	5.4 Å

Table 3.1: Some important physical properties of caesium (Weast 1981).

worst. The safe handling of alkali metals, along with some good practical notes for caesium-compatible materials at a range of temperatures is documented in Mantell (1958).

The relationship between the temperature *T*, in Kelvin, and the vapour pressure *p*, in torr, of caesium is given by Nesmeyanov (1963):

$$\log p = 11.0531 - 1.35 \log T - \frac{4041}{T} \qquad \text{(eq. 3.1)}$$

The oven used for the caesium experiments was originally designed and built as a lithium beam source by Karaganov (1997), and later used as a potassium beam source by Stockman (1998). It was not necessary to design another oven for the present project because the materials used to construct the oven were compatible for use with caesium.

3.2.2 Oven

The oven body and top were machined from solid blocks of ingot iron A250, Grade T with purity better than 98%. The two pieces of the oven were bolted together with a knife edge sealing directly onto a highly polished surface. The oven had 5mm thick walls and an interior volume of $50cm^3$. A removable nozzle assembly allowed for different types of apertures to be used and also for the oven to be reloaded through the 1cm diameter orifice without unnecessary disassembly. Both the oven and the nozzle were independently heated by THERMOCOAX two-core heating elements (type 2NcNc Ac20) wound around the oven body and nozzle assemblies. Employing this type of heating element ensured stable heating without magnetic induction. A schematic diagram of the present oven is shown in figure 3.3. Approximately 2.6W (0.2A) was required to maintain the body at about 120^oC. The nozzle was kept at a temperature $\sim 40^oC$ higher than the body to prevent caesium from being deposited within the nozzle and clogging it. The oven and nozzle temperatures were monitored independently with two chromel-alumel thermocouples.

A number of heat shields were deployed around the oven and nozzle to reduce the amount of heat radiating into the chamber. Stainless steel foil (0.05mm thick) and

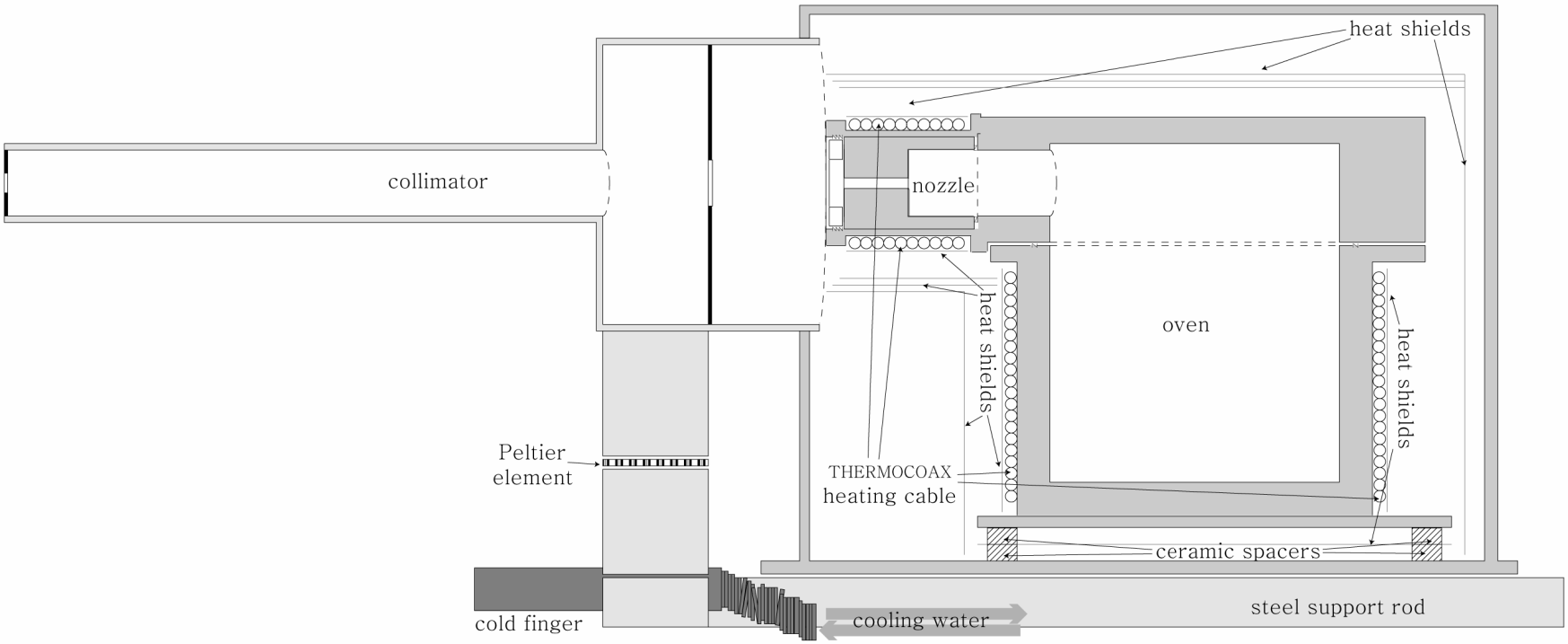

Figure 3.3: Side-view diagram of the oven, nozzle and collimator assembly (1:1 scale).

copper foil (0.1mm thick) shields surrounded both the body and nozzle. An aluminium box also enclosed the oven to protect the surrounding apparatus components in case of a leak, and to minimise the presence of any residual caesium vapour in the chamber.

3.2.3 Nozzle

The removable nozzle, having similar chemical requirements as the oven body itself, was also constructed of ingot iron A250, Grade T. The orifice measured 1.5mm x 10mm and housed a multi-channel array constructed of a single piece of corrugated tantalum foil. Early experiments were performed with the nozzle channels formed from titanium foil, but after several hours of exposure to hot caesium the titanium became brittle and failed to maintain its initial shape. However, tantalum foil had superior malleable properties and was compatible with caesium vapour and so the array was remade from tantalum.

The flow of caesium vapour through an aperture divided into a number of channel arrays was modeled following the approach of Lucas(1973). Given the vapour pressure of caesium from equation 3.1 and the geometry of the aperture, practically important parameters could then be extracted in order to investigate a range of suitable temperatures within which the beam source should be maintained. Figure 3.4 illustrates the temperature dependence of these parameters for the nozzles tested for use in the caesium superelastic experiments. When attempting to produce a high-intensity and well-collimated atomic beam it is advantageous to divide the output aperture into a series of small diameter apertures in order to improve the density of the beam at lower operating temperature and to also achieve a lower angular

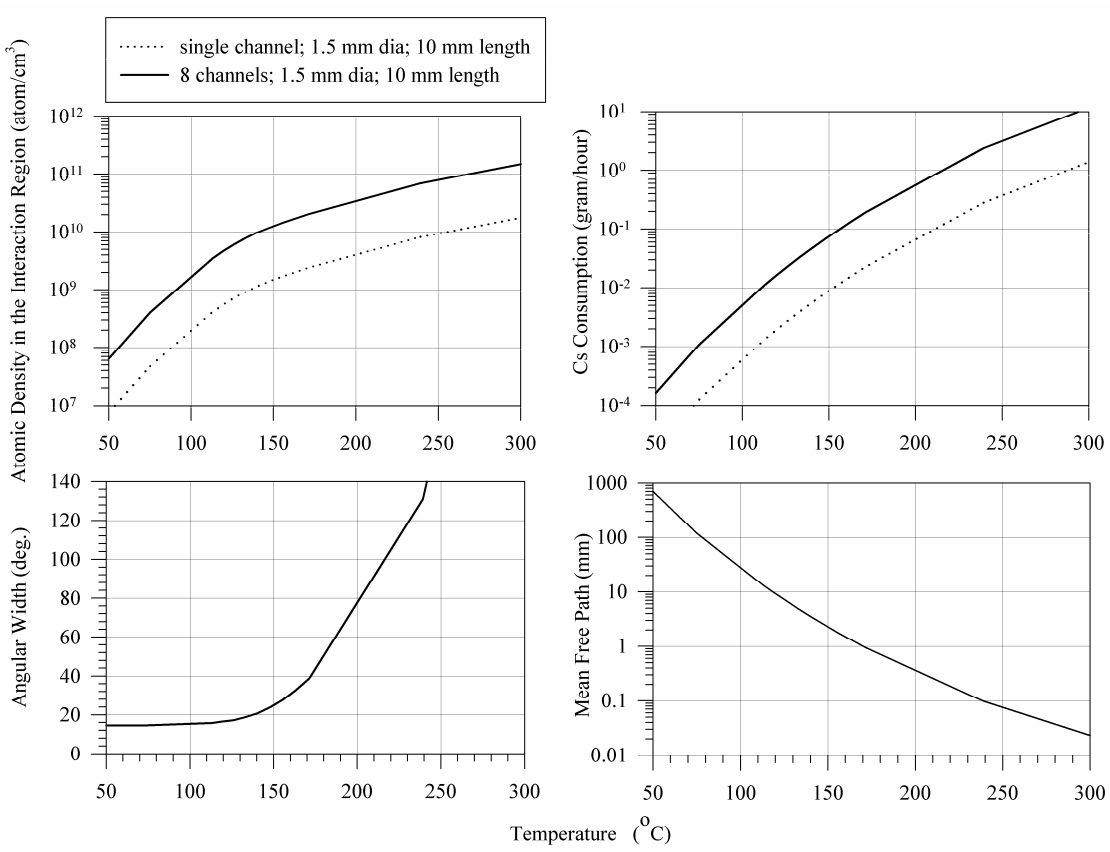

Figure 3.4: Practically important parameters of the caesium oven and the atomic beam as a function of the oven temperature for two different types of nozzle.

divergence in the atomic beam. Lucas (1973) has discussed the use of a focusing array, which reduces the angular width of the beam while increasing the beam density. A severe limitation exists, however, in the case of alkali metals such as caesium in that the hot metal vapour would tend to clog a focusing multichannel array. The same restriction was found to exist for a non-focusing multichannel array, where the diameter, and therefore the total number of channels for a given aperture, was limited by how rapidly caesium and caesium compounds were deposited within the nozzle. A compromise was therefore sought for the project and it was found that by limiting the multichannel array to 8 channels of 1.5mm diameter and ensuring that the entire nozzle was always hotter than the caesium reservoir the effective running time of the oven was approximately 100 hours. Experimental observations

confirmed that the modeled data of figure 3.4 were accurate. Therefore the running temperature of the oven was typically maintained at 118^{o}C, in order to achieve optimal atomic densities and a beam of low angular divergence, while maintaining a reasonable caesium consumption rate of around 10^{-2} g/hour.

3.2.4 Collimator and Atomic Beam Dump

As shown in the results of figure 3.4, the calculated angular width of the atomic beam as it emerges from the nozzle is still relatively large, so it was necessary to use a collimator to restrict the beam to a narrow divergence. This was important as it was found that optimal optical pumping and therefore the maximum excited state population of the caesium atoms required the production of a well collimated atomic beam.

Doppler broadening of the transition frequency within the atomic beam depends strongly on the angular divergence of the beam. The following description follows the analysis of Karaganov (1997). Any velocity component of the caesium beam in the direction of laser propagation results in a shift of the effective transition frequency due to the Doppler effect (Gerritsen and Nienhuis, 1975) (see figure 3.5):

$$\nu_{shifted} = \nu_0(1 \pm \frac{v_{atom}}{c}\sin\frac{\theta}{2}) = \nu_0 \pm \frac{v_{atom}}{\lambda_0}\sin\frac{\theta}{2} \qquad \text{(eq. 3.2)}$$

where $\nu_{shifted}$ is the Doppler shifted frequency, ν_0 is the Doppler free frequency, v_{atom} is the velocity of the atomic beam, c is the speed of light and θ defines the divergence of the atomic beam. The Doppler spread in the effective transition frequency should be smaller than the natural line width $\Delta\nu_{nat} = \frac{1}{2\pi\tau} = 5.2MHz$,

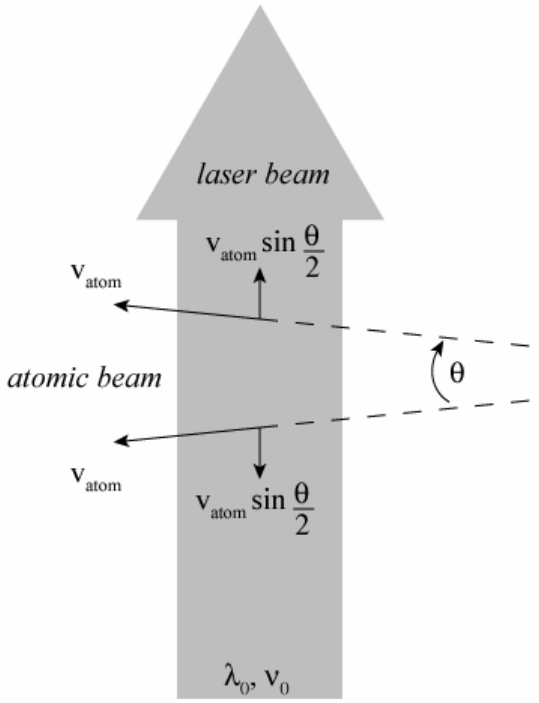

Figure 3.5: The influence of the angular divergence of the atomic beam on the effective transition frequency of the caesium atoms due to the Doppler effect.

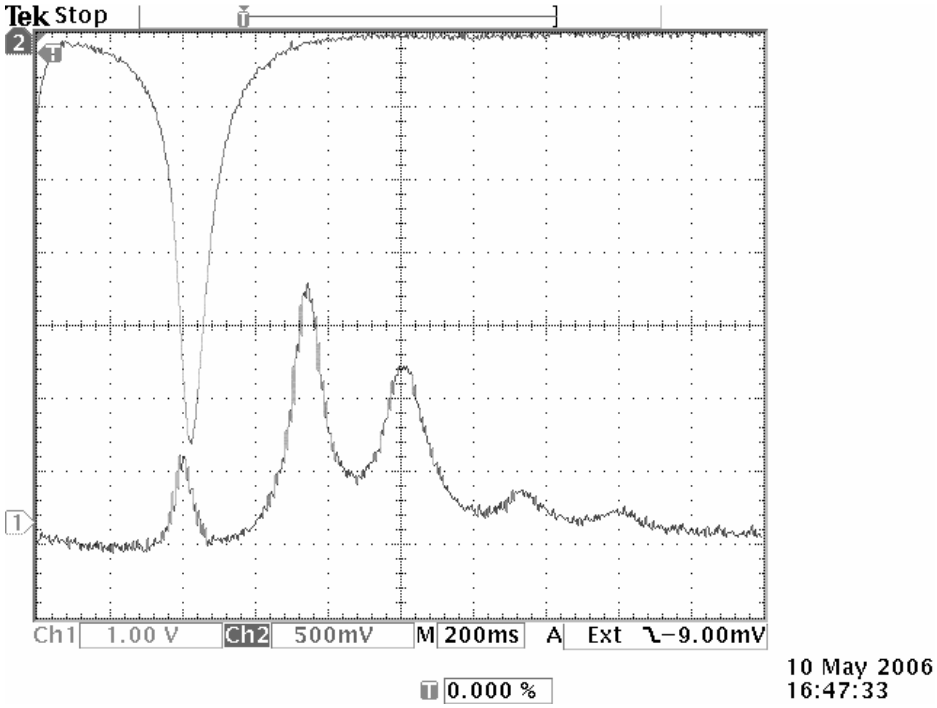

Figure 3.6: Caesium fluorescence signal (upper trace) as a function of laser detuning, showing a saturated linewidth of 40MHz for the atomic beam produced under typical operating conditions. Horizontal scale is 75MHz/division, as measured using the separation of hyperfine structure resonances, deduced from the saturated absorption spectrum (lower trace) using a caesium vapour cell.

where $\tau = 30.7ns$ (Hansen, 1984) is the lifetime of the $6P_{3/2}$ excited state in caesium. This condition maximises the number of atoms undergoing optical pumping. In practice, the high power of the laser results in a power broadened or saturated linewidth which is much wider (see figure 3.6). Thus it is desirable to constrain the atomic beam so that its Doppler width is narrower than the saturated linewidth:

$$\Delta\nu_{doppler} = 2\frac{v_{atom}}{\lambda_0}\sin\frac{\theta}{2} \leq \Delta\nu_{saturated} \qquad \text{(eq. 3.3)}$$

It was found that an atomic beam angular width of better than 7.8^o was required for a saturated linewidth of $\Delta\nu_{saturated} = 40MHz$ (full width at half maximum), laser wavelength $\lambda_0 = 852.346nm$ and mean atomic velocity $v_{atom} = 250ms^{-1}$ for an oven temperature of 120^oC.The atomic beam collimator shown in figure 3.7 was constructed from stainless steel with a 3.0mm x 5.0mm aperture at the output end. Angular divergence of the atomic beam was reduced to 2.1^o, corresponding to a Doppler spread of 10.6MHz, which was well within the experimental requirements. The temperature of the collimator body was maintained at around -8^oC by a water-cooled Peltier element, in order to ensure that excess caesium vapour was condensed inside the collimator and not introduced to the surrounding apparatus. It was also essential to protect surfaces of the apparatus from contact with the atomic beam after it passed through the interaction region (see section 3.2.5). Any brass or stainless steel surfaces which were exposed to caesium vapour tended to swiftly form an oxide coating which could potentially become electrically charged during the experiment. An atom trap **(**see figure 3.2**)** was therefore designed in order to prevent the surfaces of the electron gun and electron analyzer from becoming contaminated

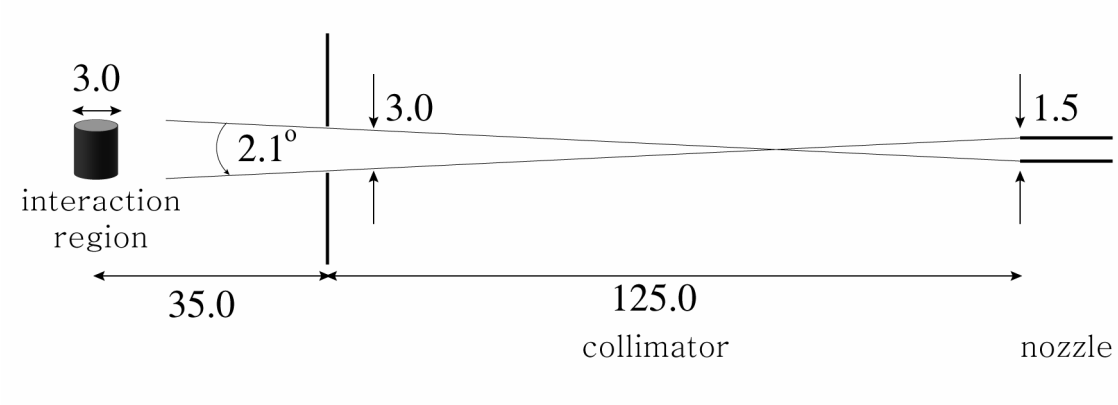

Figure 3.7: A schematic illustration of the atomic beam collimator used in the present experiments (not to scale), viewed in the scattering plane. Also illustrated is the atomic beam intersection with the laser (the interaction region). All lengths are in mm.

with caesium, particularly when they were positioned in or near the atomic beam path. The present trap essentially consisted of a 30mm x 15mm copper plate supported by a copper arm and positioned directly opposite the collimator output. The entire assembly was cooled by the same Peltier element employed for cooling the collimator.

3.2.5 The Interaction Region

Due to the three-beam nature of the superelastic electron scattering experiments, it was essential to have a clearly defined target scattering region. This volume, which shall be referred to as the *interaction region*, was defined as the intersection of overlap between the atomic beam and the laser beam (see figures 3.2 and 3.5). It was therefore possible to control not only the volume, but also the exact position of the interaction region by simply controlling the diameter and position of the laser beam. Typically, the interaction region was confined to a volume of $35mm^3$, by restricting the laser beam diameter to 3mm for a nominal caesium atomic beam divergence of 2.9^o.

3.2.6 Operation

Special techniques have been developed for the safe handling and preparation of caesium for study in the laboratory (see, for example Brotherton *et. al.* (1962), Mantell (1958) and Perel'man (1965)). The procedures employed in the present experiments were developed from earlier work with alkali metals at Flinders (Karaganov *et. al.* 1999) along with the handling methods of Brotherton *et. al.* (1962).

Caesium ingot was supplied for the present project in conveniently-sized 1g ampoules surrounded by fire-retardant packing in a steel canister. It was necessary, when loading caesium into the oven, to hold both the oven and all the handling tools under an argon environment. This was required in order to prevent caesium from oxidising before the oven was placed inside the scattering chamber and evacuated. Working within the argon filled dry box, the metal was warmed to approximately 35^{o}C (see table 3.1) so that the entire contents of an ampoule could be readily transferred, by teat pipette, through the nozzle aperture and into the oven reservoir. With the nozzle replaced, the oven was then sealed and carefully transferred from the dry box and secured inside the scattering chamber. An argon injection line inside the scattering chamber to the atomic beam collimator ensured that the reservoir was held under inert conditions until the chamber could be evacuated.

A typical reservoir temperature of 118^{o}C resulted in a partial pressure of 3.5×10^{-3} torr (Nesmeyanov, 1963) and an atomic density of $\sim 3 \times 10^{9}$ atoms/cm^{3} (see figure 3.4) at the interaction region. This temperature was maintained for each experimental run. It was found that lower oven temperatures would result in a

reduced superelastic count rate due to lower target density, while higher temperatures would consume the small sample of caesium too rapidly. Under optimal conditions, 1g of caesium would last for up to 100 hours of operation, which was one of two limitations to the duration of an experimental run. The other limitation was, in spite of our precautions, the tendency for the nozzle to become clogged with caesium, thus reducing its performance, after repeated heating and cooling of the oven and many hours of operation. A summary of the practically important characteristics of the atomic beam apparatus is presented in table 3.2.

atomic beam	
mean velocity of atoms	250 $m.s^{-1}$
density of atoms at the interaction region	$3 \times 10^9 - 5 \times 10^9$ $atoms.cm^{-3}$
beam divergence (FWHM)	2.9^o
Distance from the collimator to the interaction region	35 mm
caesium oven	
oven material	ingot iron A250 grade T
capacity	50 cm^3
operating temperature	120 ^oC
approximate running time	over 100 hours
removable nozzle	
nozzle materials	ingot iron A250 grade T, tantalum foil
aperture diameter	1.5 mm
aperture length	10 mm
operating temperature	160 ^oC
collimator	
length	125 mm
aperture	2.5 mm x 5.0 mm
operating temperature	-8 ^oC

Table 3.2: Atomic beam parameters of practical importance.

3.3 Electron Gun and Spectrometer

3.3.1 Electron Gun

An electron gun, originally built by Scholten (1989) for superelastic scattering experiments with sodium, was successfully used throughout the caesium superelastic experiments. Prior to its implementation in the current project, it was modified by Karaganov (1997) for superelastic scattering from lithium and later used by Stockman (1998) for studies on potassium. The current version of the gun is shown in figure 3.8.

The electron gun was constructed as a series of electrostatic lenses from the data of Harting and Read (1976). The lenses were fabricated as discs from 0.15mm thick molybdenum shim, with each element separated by 1mm thick rings of macor (machinable ceramic) and 310 stainless steel tube. The apertures, spacers and deflector assemblies were stacked between four macor supporting rods and pulled together with two retaining rods. A Pierce stage extracted electrons from the indirectly heated cathode and lens L1 focused them into a beam and onto the collimating apertures A1 and A2. Two sets of four-plate deflectors (D1 and D2) were employed to guide the electron beam through the gun. Voltages on the final lens system L2 and final deflector D3 were adjusted to further collimate and direct the beam onto the interaction region. Zero beam angle at the interaction region was an important criterion that was maintained throughout the present experiments, with the aid of a pair of Faraday cups, as described in section 3.3.2.

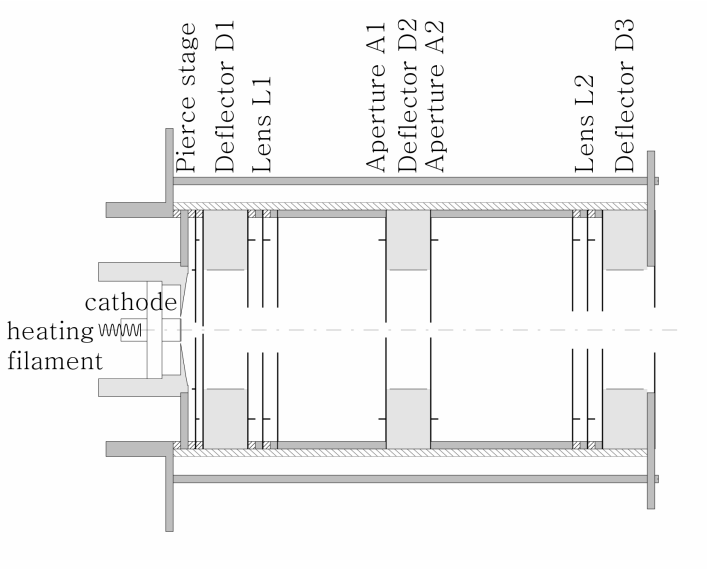

Figure 3.8: Schematic diagram of the electron gun (1:1 scale).

The electron source consisted of an indirectly heated barium oxide cathode (Centronix, Model 1/2 C60-490 6.3 600-E-D-100). The cathode voltage was applied directly to the molybdenum cap on which the oxide was coated. This type of cathode has an operating temperature of less then 1000^{o}C, which corresponds to a minimal electron thermal energy spread $\Delta E_{thermal} \approx 0.3eV$ (Simpson 1967). However, a problem became apparent when it was discovered that a contact potential exists between the cap and the oxide coating, causing a shift between the applied voltage and the electron beam energy. This problem, along with the calibration technique that was employed to overcome it, is discussed further in section 3.3.5.

3.3.2 Electron Beam Characteristics

A pair of concentric Faraday cups was in place to monitor the electron beam current and profile. The cups were constructed of brass, with each rim machined to a knife edge and the entire cup assembly surrounded by a copper shield. The surface of each cup was coated with a graphite coating to facilitate the rapid removal of any build-up of electrostatic charge. The Faraday cup assembly was mounted on an aluminium

stand which could be positioned at a convenient location within the scattering chamber, usually at a reasonable distance from the interaction region.

Both the diameter and angular divergence of the electron beam could be determined by observing the inner cup current as the beam was scanned across it. The beam was scanned either by rotating the gun turntable or alternatively by adjusting the potential across two of the deflector plates on the final deflector D3. Given the inner Faraday cup diameter of 4mm the angular resolution of our divergence measurements was approximately 1^{o}. Typically, the beam diameter was 4mm and the angular divergence ranged from 4.5^{o} at 7eV to 2.5^{o} at 15eV, which ensured that the beam was larger than the interaction region. Electron beam currents were around $0.1\mu A$ at 7eV and $0.3\mu A$ at 15eV. Once a stable beam was produced at a given energy, the electron gun was usually left running for many hours of operation and it was generally found that stability improved further with running time. While each cathode normally had a lifetime of well over 100 hours of operation, they were rendered inoperative after exposure to atmosphere once activated. Hence it was standard practice to dismantle and clean the gun after each experimental run and to replace the cathode.

3.3.3 Scattered Electron Energy Analyser

The superelastic electron scattering project required a method of not only detecting superelastically scattered electrons, but also discriminating them from the lower energy elastic and inelastic scattered electrons. The retarding field analyser (RFA) originally designed by Scholten (1989) was found to be well suited for this task.

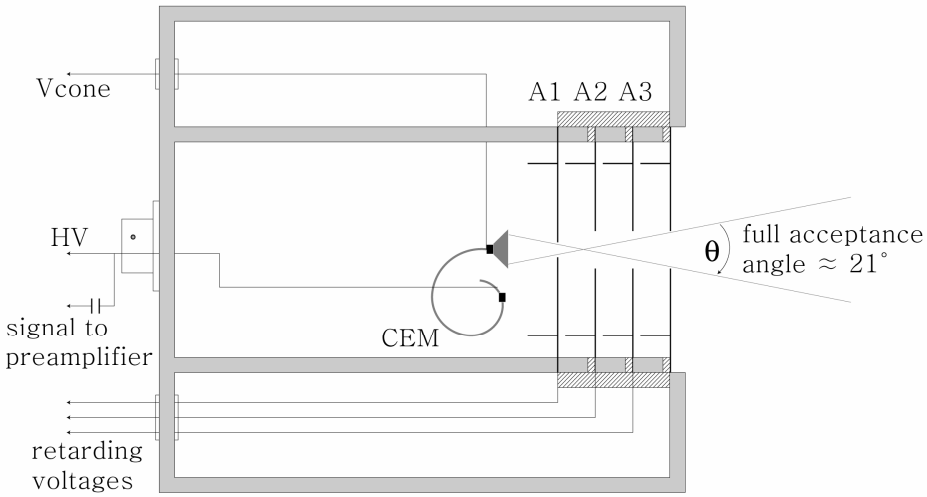

Figure 3.9: Schematic diagram of the present retarding field electron analyser (1:1 scale).

An RFA consists of an electrostatic lens which essentially focuses an image of the interaction region onto a detector, while rejecting electrons below a well- defined threshold energy. The RFA which was used throughout the present experiments is shown in figure 3.9. This RFA's full acceptance angle, θ, was measured to be about 21^{o}, which was adequate for the current experimental geometry. It is noted that, since the RFA is designed to reject elastically scattered electrons, the only requirement with respect to the acceptance angle was that it was wide enough to view the entire interaction region.

The retarding voltage placed on each lens element was adjusted in order to achieve maximum energy resolution. In practice this was accomplished by repeatedly scanning the analyser reference voltage across the elastic threshold and observing the elastic cutoff curve measured by the detector. The voltage applied to each aperture A1, A2, A3 and to the front of the channel electron multiplier (V_{cone}) was optimised in order to produce a cutoff curve closely resembling a step-function. The

energy resolution of the analyser could then be determined by differentiating the cutoff curve and measuring the full width at half maximum (FWHM) of the resulting peak. A typical elastic cutoff curve and the corresponding electron energy distribution are shown in figure 3.10. In addition, typical analyser optimised potentials are shown in table 3.3. A channel electron multiplier (CEM, Mullard B318BL) was used to detect electrons above a nominated energy, which was set using the retarding voltages of the electrostatic lens.

3.3.4 Data Acquisition

Pulses produced from the electron analyser were amplified by an ORTEC 113 preamplifier and ORTEC 460 delay line amplifier. It was necessary to discriminate the pulses from low level background noise and this was accomplished using a single channel analyser (ORTEC 551). Finally, each pulse was counted and recorded via a multifunction I/O board (National Instruments PCI-6024E) mounted in a PC using National Instruments LabVIEW software, developed as part of this project. A schematic diagram of the electron scattering data acquisition apparatus is shown in figure 3.11.

3.3.5 Electron Beam Energy Calibration

The electron beam energy was selected by applying a voltage directly to the cathode cap. Since electrons were emitted from the surface of an oxide coating on the cap, it was soon realised that the beam energy would depend not only on the cathode voltage, but also on the contact potential between the oxide and the cap. The contact potential itself varied from between one to two volts and generally depended on the operating temperature of the cathode, and therefore the heating filament current, as

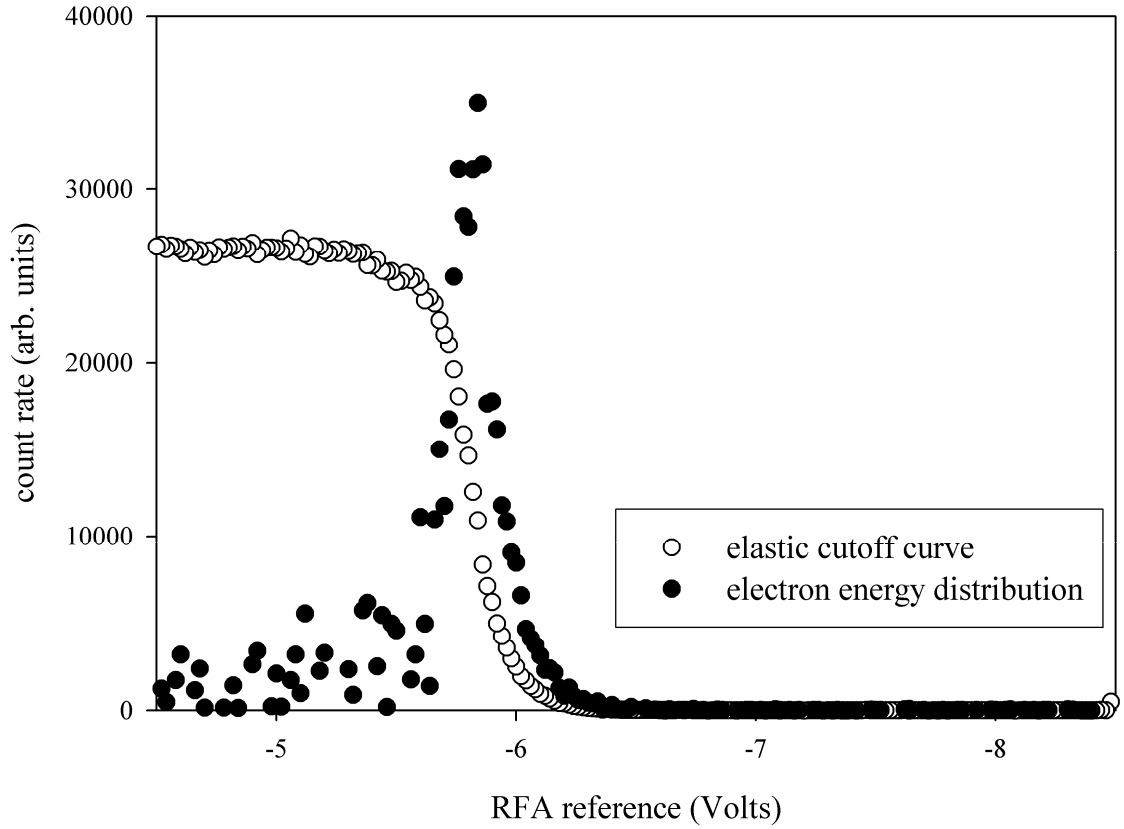

Figure 3.10: Typical elastic electron cutoff curve, o*, and its corresponding electron energy distribution (differentiated cutoff curve),* •*, for a nominal 5.5eV electron energy.*

incident electron energy	**V_{cone} (V)**	**A1 (V)**	**A2 (V)**	**A3 (V)**
5.5eV	-1	x	x + 1.0	x + 3.5
8.5eV	-1	x	x + 0.8	x + 5.0
13.5eV	-1	x	x + 0.4	x + 8.0

Table 3.3: Typical optimised analyser potentials (in Volts) for various electron energies. 'x' denotes the RFA reference potential.

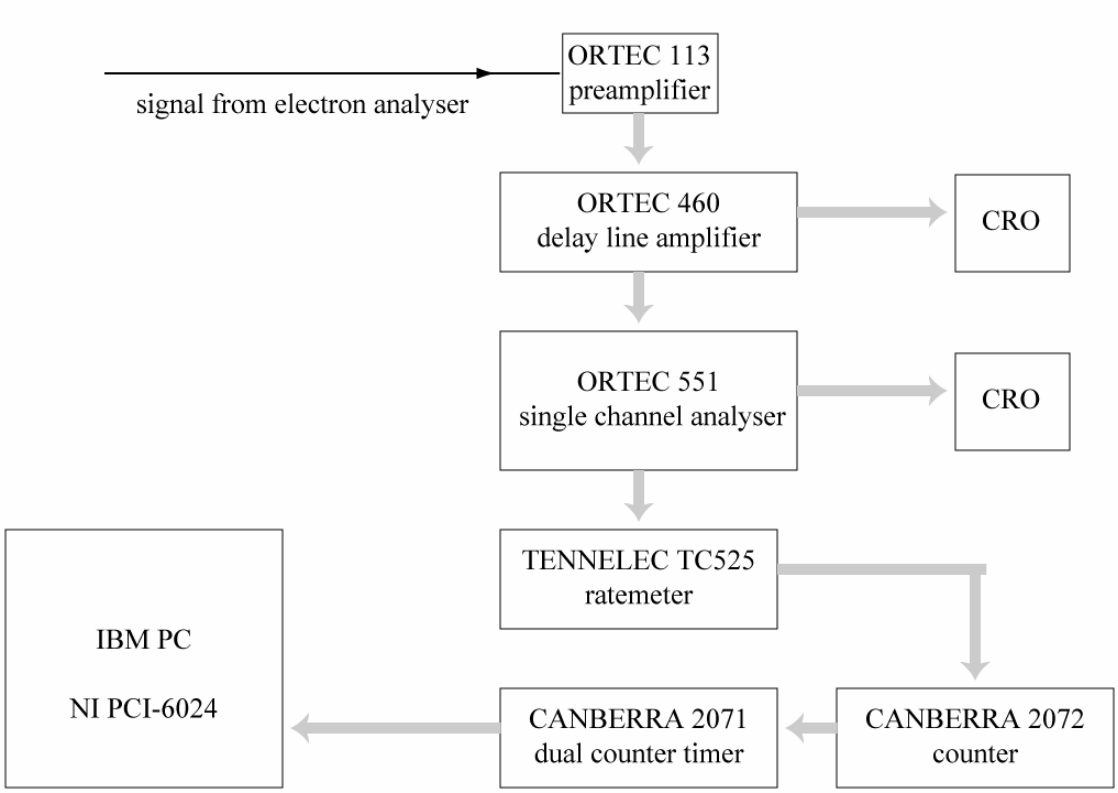

Figure 3.11: Schematic of the electron scattering data acquisition system.

well as the history of the cathode itself. A calibration procedure was therefore employed to compare the apparent beam energy with a known feature in order to determine the oxide cathode contact potential at any time during an experiment. The so-called b-feature in the excitation function of metastable neon (Buckman *et al.* 1983), at 16.91eV, was used as the standard for each energy calibration of the electron beam. A nozzle situated near the chamber wall produced a beam of neon atoms directed at the electron analyser, which was set to completely reject electrons and instead detect only metastable neon atoms. The electron energy was scanned using the electron gun programmable power supply in order to measure the excitation rate of metastable neon atoms in the neon beam as a function of electron energy. This procedure was independent of electron gun position and, due to the compatibility of neon with caesium, could be conveniently performed at any time

during a superelastic scattering experiment. The uncertainty in the energy calibration procedure was estimated to be typically $\pm 0.06\,\mathrm{eV}$. The equivalent Stokes parameters were observed to be highly sensitive to electron energy (see chapter 6) and hence it was particularly important that the beam energy was known and fixed throughout a series of measurements. Typically the electron beam energy was calibrated before, after and at various stages throughout an experimental run in order to eliminate any possibility of drift in electron energy. In most circumstances the cathode contact potential was found to be constant, indicating that the electron beam energy was stable for many hours of operation, provided that a constant cathode heating current was maintained. A summary of the main operational characteristics for the electron gun and electron analyser is given in table 3.4.

electron gun	
extraction type	Pierce stage
cathode type	barium oxide, indirectly heated
cathode operating temperature	1000 ^{o}C
thermal energy spread	0.3 eV
electron analyser	
type	focusing, retarding field analyser
detector	channel electron multiplier
typical electron beam parameters	
typical beam current at 10eV	200 nA
typical beam divergence at 10eV (FWHM)	3.0^{o}

Table 3.4: Electron beam source and detector parameters.

3.4 Laser System and Optics

3.4.1 Diode Laser Source

It is crucial to have a frequency stabilised source of laser radiation so that an atomic target can be prepared in a well defined excited state for the whole period of an experiment. In the case of the caesium project it was also desirable to have a continuous-wave, narrow bandwidth, frequency tunable laser which was able to operate reliably at 852.346nm. A tunable single frequency extended cavity diode laser (TuiOptics DL100) successfully met these requirements and was used throughout the project. The system consisted chiefly of an extended cavity laser diode in a Littrow grating arrangement (see Demtroder 1996), that was driven by a regulated DC power supply (TuiOptics DCC100) and temperature stabilised by a thermoelectric element (TuiOptics DTC100). A piezoelectric element attached to the Littrow grating was driven by a separate supply (TuiOptics SC100), which was interfaced to the DCC100 supply via the DL100 backplane bus. Thus by controlling the angle of the grating with respect to the diode end facet, while simultaneously tuning the diode driving current, the laser could be frequency tuned and modulated with minimal mode-hopping.

3.4.2 Frequency Stabilisation

A feedback signal was required to lock the laser frequency to the desired transition in caesium. While the hyperfine energy level splitting in the $6^2P_{3/2}$ excited state is a few hundred Megahertz, the Doppler broadening due to the velocity distribution of atoms at normal room temperature is much wider, resulting in the excited state hyperfine structure being unresolved. Therefore a technique employing Doppler-free

spectroscopy was required in order to provide a frequency dependent feedback signal which was sensitive enough to maintain the laser frequency at a specific hyperfine transition. The technique commonly known as saturated absorption spectroscopy was chosen for this task.

The detailed principles behind saturated absorption spectroscopy have been reported elsewhere (see for example Demtroder 1996) and therefore the following description of the technique will be limited to a practical perspective. A small portion of the plane-polarised laser beam is directed at beam splitter S1 (see figure 3.12) toward the saturated absorption apparatus. Weak reference and probe beams, originating from S2 and S3 respectively, are then separated from the pump beam and propagate through the caesium vapour cell. The pump beam is directed through the vapour cell such that both pump and probe beams overlap spatially, but propagate in opposite directions. If the laser frequency, ω_0, corresponds to a resonance transition of caesium then those atoms in the path of the pump beam will be pumped into the upper level of that transition, leaving a smaller population of atoms residing in the lower level. It is important to note that the caesium vapour atoms have a range of velocities given by their Maxwell-Boltzmann velocity distribution, and any atom with velocity v_z in the direction of propagation (defined as the z-direction) will be pumped due to the Doppler-shifted laser frequency in the frame of the moving atom:

$$\omega' = \omega_0 \pm kv_z \qquad \text{(eq. 3.4).}$$

When the much weaker probe beam is directed along the same path, but in the opposite direction to the pump beam, it will detect a decrease, or saturation, in absorption only for the group of atoms with velocity component $v_z = 0$. Thus, by

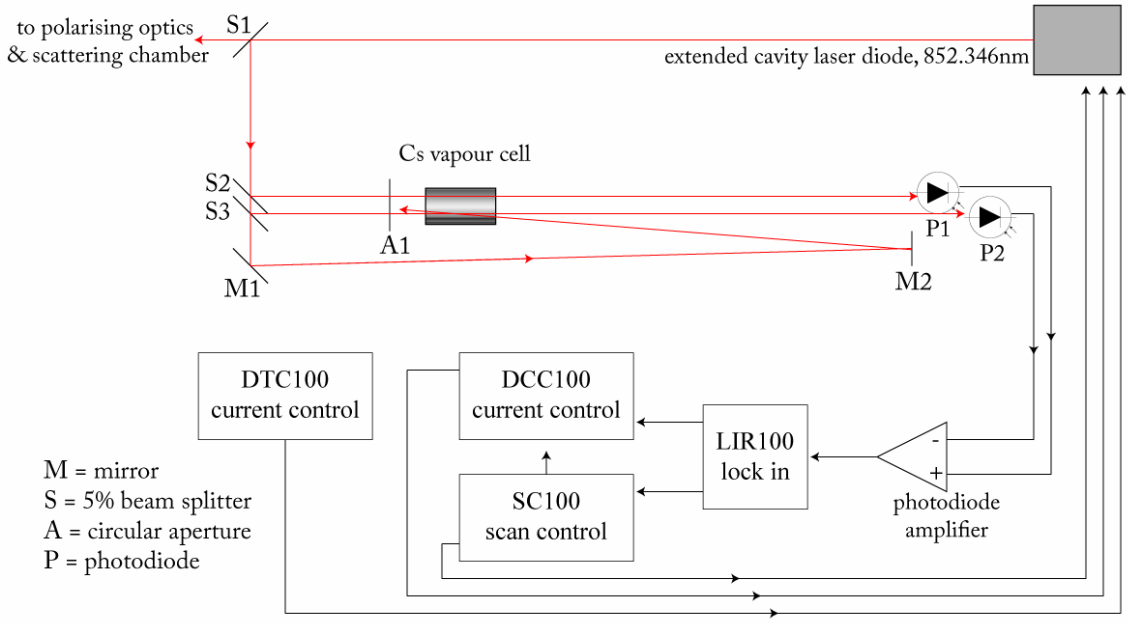

Figure 3.12: Schematic diagram of the frequency stabilisation experimental setup.

measuring the probe beam intensity while scanning the laser frequency, one can detect a sharp resonance due to an atomic transition, while excluding all atoms that are not moving in the plane perpendicular to the pump and probe laser propagation. When the full Doppler spectrum of the reference beam is subtracted from the probe beam signal something closely resembling a Doppler-free absorption spectrum is revealed (see figure 3.13). By monitoring the saturated absorption signal on a digital oscilloscope, the laser frequency could be tuned to the desired peak. However, as mentioned earlier, an active feedback system was required in order to ensure long term frequency stability. Accordingly the saturated absorption signal was fed to the laser lock-in (TuiOptics LIR100), which mediated the outputs of the current and scan controllers of the laser, correcting both for any long term frequency drift and vibrations. Typically, within stable laboratory conditions, the laser frequency could be held precisely to the desired transition for as long as 48 hours.

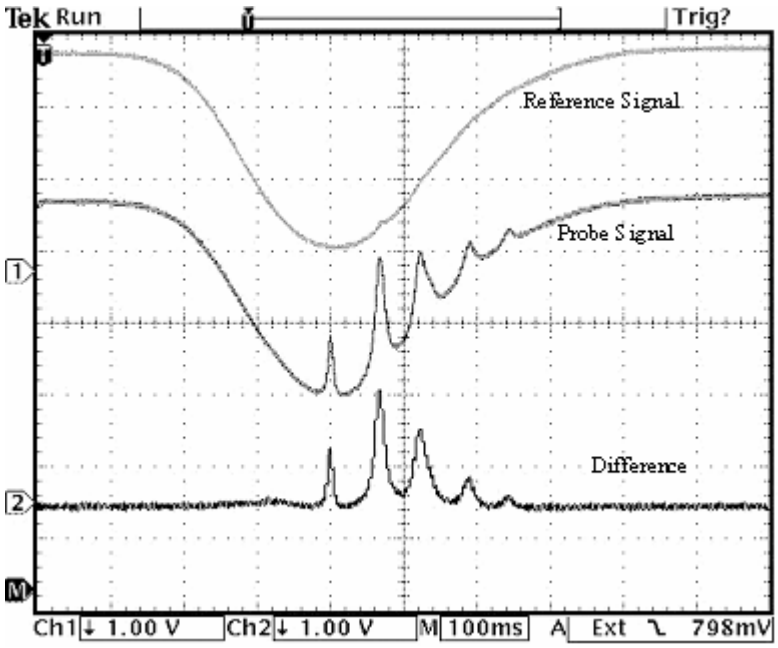

Figure 3.13: Saturated absorption spectrum for the caesium D_2 transition. The Doppler-free spectrum (lower trace) is obtained from the subtraction of the measured reference beam intensity (upper trace) from the probe intensity (middle trace). Note that not all peaks correspond to a transition; so called cross-over peaks (Demtroder 1996) occur between every pair of resonance peaks.

3.4.3 Polarising Optics

The superelastic experiment required a polarimeter which was capable of accurately producing linearly polarised light at any angle or circularly polarised light of either helicity, without addition or removal of any optical components. This would ensure that a complete set of equivalent Stokes parameters could be measured in a single experimental run. Such a polariser was first reported by Karaganov *et. al.* (1996) and this same polarimeter was employed for the present caesium superelastic scattering experiments. It consists of two identical zero-order quarter wave plates (Melles Griot 02WRQ007) mounted in rotating stages, run by two stepper motors (SLO-SYN M061) which are driven by computer control. This arrangement enabled changes in the polarisation axis to within $\pm 0.3°$, while maintaining the same alignment and intensity of the laser beam. The arrangement, along with the relevant

configurations for each of six polarisation states, is illustrated in figure 3.14. The polarisation of a beam of light can be conveniently described by four independent parameters, as first established by Stokes (1852):

$$S = \begin{pmatrix} S_0 \\ S_1 \\ S_2 \\ S_3 \end{pmatrix} \qquad \text{(eq. 3.5)}$$

Each of the parameters S_n can be determined from simple measurements (Shurcliff 1966):

$$\begin{aligned} S_0 &= I(0^o) + I(90^o) \\ S_1 &= I(0^o) - I(90^o) \\ S_2 &= I(45^o) - I(135^o) \\ S_3 &= I(RHC) + I(LHC) \end{aligned} \qquad \text{(eqs. 3.6),}$$

where $I(\phi)$ represents the intensity of the component of light with electric field vector oriented at ϕ^o for linearly polarised light or left handed or right handed orientation in the case of circularly polarised light (denoted LHC or RHC respectively). Within this treatment it becomes clear that S_0 characterises the total radiation intensity, while S_1 and S_2 characterise the degree of linear polarisation of the beam. Similarly S_3 indicates the degree of circular polarisation. In the case of monochromatic light, only three of the four parameters are independent. By making use of the formula:

$$\left(\frac{S_1}{S_0}\right)^2 + \left(\frac{S_2}{S_0}\right)^2 + \left(\frac{S_3}{S_0}\right)^2 = 1 \qquad \text{(eq. 3.7),}$$

the degree of linear polarisation can be determined by,

$$S_{linear} = \sqrt{\left(\frac{S_1}{S_0}\right)^2 + \left(\frac{S_2}{S_0}\right)^2} \qquad \text{(eq. 3.8)}$$

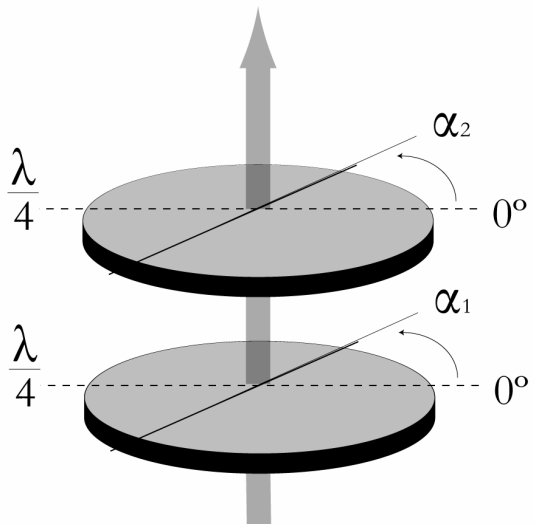

laser polarisation	α_1	α_2
RHC	0^o	45^o
LHC	0^o	-45^o
0^o	45^o	-45^o
45^o	45^o	0^o
90^o	45^o	45^o
135^o	45^o	90^o

Figure 3.14: Polarimeter consisting of two quarter wave plates. Six different polarisation states can be achieved by selecting the orientation of each plate, as shown in the table. The laser beam is initially linearly polarised, oriented at 0^o.

and the degree of circular polarisation by,

$$S_{circular} = \frac{S_3}{S_0} \qquad \text{(eq. 3.9).}$$

Thus the degree of polarisation can be determined by simple measurements using a polariser and power meter at any point along the beam path.

It was found that imperfect laser polarisation resulted in inaccurate experimental results for the caesium superelastic scattering experiments. While setting up an experiment, the final polarisation state of the laser beam was measured for each configuration of the optical components. Typical measured values for the linear and circular polarisation components were 0.9995 and 0.9993 respectively. As an example, for the case of linear polarisation, this indicates an undesired circular component of $\sqrt{1\text{-}0.9995^2} = 0.032$. Further investigations attributed the polarisation errors to a combination of three sources: the birefringence of the vacuum windows,

the tolerance of the two quarter-wave plates of $\pm\lambda/250$ (Melles Griot specification) and the tolerance of the rotating stages ($\pm 0.3^{o}$). The influence of these uncertainties on the experimental results is discussed in chapter 5.

3.4.4 Fluorescence Detection

A photodiode detector was installed on a side window of the scattering chamber, parallel to the laser beam axis and in the scattering plane, so that the optical pumping performance of the laser system and the atomic beam could be determined. A photographic zoom lens (Tokina ATX-828(SD) focal length: 80-200mm) was employed in front of the detector to magnify the image of the interaction region. An analysing polariser (Newport 05P109AR) placed after the lens enabled polarisation analysis of the fluorescence radiation.

3.4.5 Additional Optical Components and Instrumentation

Some additional optical components were employed along the path of the laser beam, in order to improve experiment operational conditions. These included a Glan-Taylor polariser immediately before the polarimeter, which effectively removed any elliptical component of the beam due to reflections from the mirrors. A circular iris aperture was also employed in order to ensure a symmetrical beam profile. Since the interaction region was defined as the intersection of the atomic beam and the laser, this variable-diameter aperture also enabled the volume of the interaction region to be controlled.

Other essential instruments which were required throughout the experiments included a wavemeter (Burleigh WA20), capable of measuring wavelengths to an accuracy of $\pm 0.001\,\text{nm}$. A spectrum analyser (TechOptics SA2) was also useful for

viewing the laser mode structure. A variable attenuator/beamsplitter (Newport 50G02) and a set of neutral density filters (Oriel) were further used in order to control the laser intensity. A summary of the current laser system parameters is provided in table 3.5.

laser diode	
model	SDL5411-G1
threshold current	15 mA
typical operating current	94 mA
mode-hop-free scanning range	10 GHz @ 84 mA, 20.7 ^{o}C
Littrow grating	1800 lines/mm
frequency control	
feedback system	saturated absorption spectroscopy arrangement
lock-in	TuiOptics LIR100
polarimeter	
quarter-wave plates	Melles Griot 02WRQ007, $\pm\lambda$/250 retardation tolerance
Stepper motor/rotation stage	SLO-SYN M06, 0.2 degree/step
typical laser beam parameters	
output power	64 mW
operating wavelength	852.346 nm
beam diameter	3 mm (Gaussian profile)

Table 3.5: Summary of the laser system parameters.

4 Optical Pumping

4.0 Introduction

Caesium has a single naturally occurring isotope, ^{133}Cs, which has a nuclear spin angular momentum of $I = 7/2$, while the valence electron has a total angular momentum of $J = 1/2$ and $J = 3/2$ for the $6^2S_{1/2}$ and $6^2P_{3/2}$ states, respectively. The interaction between the nuclear spin and the electron angular momentum produces a hyperfine structure which is illustrated in figure 4.1. Each energy level within the hyperfine structure is labeled by the quantum number $\overline{F} = 3,4$ and $F = 2,3,4,5$ for the $6^2S_{1/2}$ and $6^2P_{3/2}$ levels, respectively, and each hyperfine energy level is further divided into $2F+1$ degenerate sublevels. The convention of representing the ground state quantum numbers with an over-bar (eg. $\overline{F}$) will be used throughout this chapter to distinguish the lower and upper level quantum numbers.

Optical pumping is a well established technique whereby an atomic target can be prepared in a well defined quantum state through repeated excitation and spontaneous decay using polarised light. Experiments as early as the 1950s (see, for example, Franzen and Emslie, 1957) demonstrated this highly effective method for atomic orientation with the alkalis. Since such early work, progress and refinement in spectroscopic techniques along with better coherent sources of light have enabled optical pumping to become one of the most powerful tools in the superelastic experiment.

4.1 Preparation of the Caesium Target

In general, the superelastic experiment requires a stable two-state atomic target. Absorption of resonant radiation tuned to the $6^2S_{1/2}\ \overline{F}=4 \rightarrow 6^2P_{3/2}\ F=5$ transition by the ground state caesium atoms results in a fraction of their total population being excited to the upper state. In the present superelastic experiments, the diode laser system is frequency-locked to this transition (as illustrated in figure 4.1). Provided the frequency of this transition is well-resolved with respect to the surrounding hyperfine structure, light-induced electron excitation occurs only within these two energy levels. The excitation process itself is governed by the following selection rules under the dipole approximation (Sobel'man 1972):

$$\begin{aligned} &\Delta L = \pm 1 \\ &\Delta F = 0, \pm 1,\ \Delta M_F = 0, \qquad \text{when } M_F \neq 0 \\ &\Delta F = \pm 1,\ \Delta M_F = 0, \qquad \text{when } M_F = 0 \end{aligned} \qquad \text{(eqs. 4.1)}$$

for transitions induced by linearly polarised light and,

$$\begin{aligned} &\Delta L = \pm 1 \\ &\Delta F = 0, \pm 1 \\ &\Delta M_F = \pm 1 \end{aligned} \qquad \text{(eqs. 4.2)}$$

for transitions induced by circularly polarised light. During the subsequent spontaneous decay the emitted light can have any polarisation, so that the selection rules are relaxed:

$$\begin{aligned} &\Delta L = \pm 1 \\ &\Delta F = 0, \pm 1 \\ &\Delta M_F = 0, \pm 1 \end{aligned} \qquad \text{(eqs. 4.3).}$$

The approximate time taken for a single atom within the atomic beam to traverse the

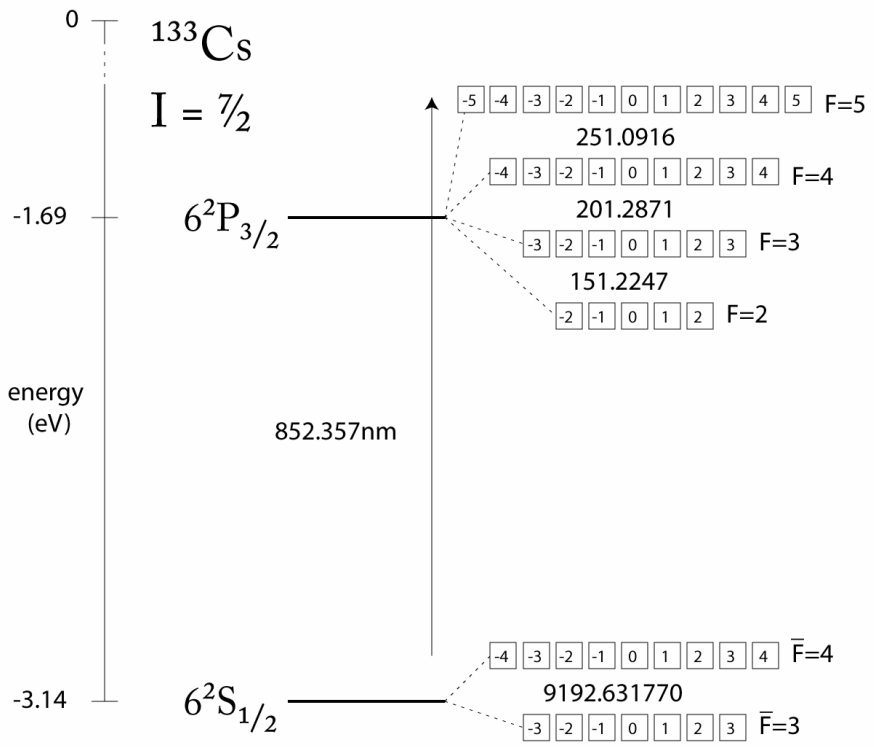

Figure 4.1: Energy level diagram for the $6^2S_{1/2}$ and $6^2P_{3/2}$ states of caesium, including hyperfine level splitting (in MHz, not to scale) and magnetic sublevels (represented by boxes labeled by quantum number M_F). Numerical data is due to Gerginov et. al. (2004).

laser field is $t = 12\mu s$ (from the data of tables 3.2 and 3.5), while the lifetime of the P-state is $\tau = 30.7ns$ (Hansen 1984). Thus many cycles of excitation and decay will occur within the atom's transit time through the interaction region. Some examples of these allowed transitions are illustrated for the caesium states of interest in figure 4.2. An immediate observation that one can draw from this picture is that, after several cycles of excitation and decay when optically pumped with right-handed (or left-handed) circularly polarised light, the target will tend to occupy only the highest sublevels, $\overline{F} = 4, \overline{M}_F = 4 \leftrightarrow F = 5, M_F = 5$ ($\overline{F} = 4, \overline{M}_F = -4 \leftrightarrow F = 5, M_F = -5$). The sublevel distribution for the case of optical pumping with linearly polarised light is not as obvious, but it is clear that the $M_F = 5$ and $M_F = -5$ sublevels are

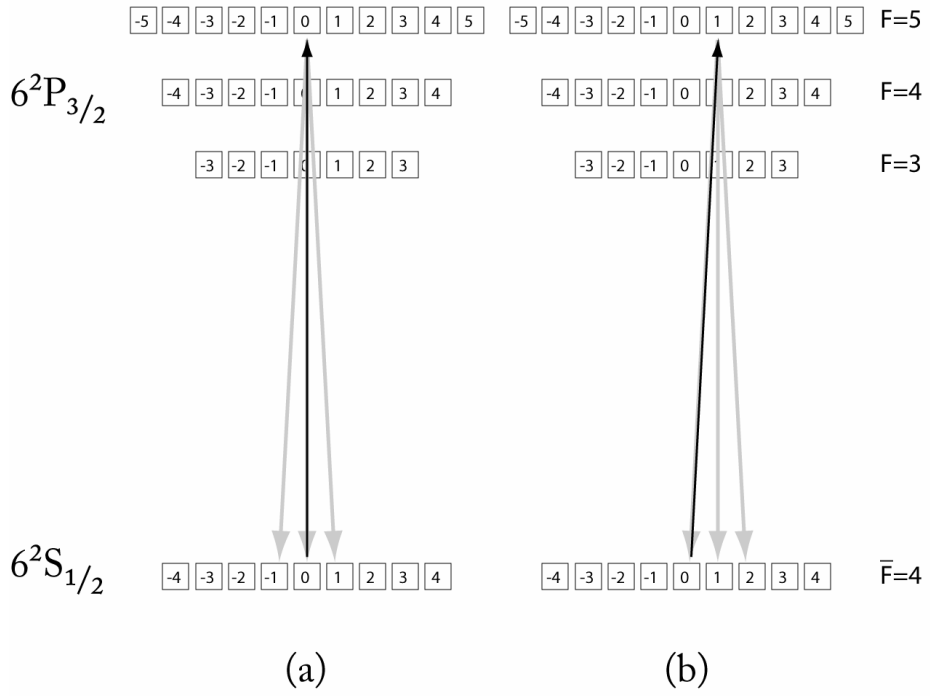

Figure 4.2: Examples of some allowed transitions between the $6^2S_{1/2}$ F=4 and $6^2P_{3/2}$ F=5 sublevels in caesium, as induced by (a) linearly polarised and (b) right-hand circularly polarised light. The subsequent decay transitions are also shown. Each magnetic sublevel is labeled in boxes by magnetic quantum number M_F.

not accessible in this case and the $M_F = 0$ sublevel will be favoured with a higher probability. Provided that the laser is tuned to the $6^2S_{1/2}\ \overline{F} = 4 \rightarrow 6^2P_{3/2}\ F = 5$ transition and the saturated linewidth is much narrower than the adjacent hyperfine splitting of the $6^2P_{3/2}$ state, the F=4 and F=5 levels of the upper state are well-resolved. Consequently the $6^2S_{1/2}\ \overline{F} = 3$ level of the ground state is effectively removed from the optical pumping process and hyperfine depopulation trapping, which has been known to introduce considerable complications in studies of the lighter alkalis (for example, see Karaganov *et. al.* 1999 and Stockman *et. al.* 1998), cannot take place. Given the relatively wide separation of the upper state hyperfine structure in this study ($251MHz$ separation for the $6^2P_{3/2}\ F = 4, F = 5$ hyperfine levels, see figure 4.2), it was expected that this condition could be achieved for the

typical saturated linewidth of $\Delta\nu_{saturated} = 40MHz$ after power- and Doppler-broadening (section 3.2.4). This expectation was confirmed experimentally, by monitoring the decay fluorescence intensity and polarisation as a function of atomic beam density. From the data of figure 4.3, the variation in the degree of fluorescence polarisation was found to be negligible for atomic densities of up to 10^{10} atoms/cm^3.

4.2 Theoretical Models of the Laser-Atom Interaction

The first quantum electrodynamic (QED) description of the interaction between light and a two-level atom was by Ackerhalt and Eberly (1974). They extended Lorentz's ideas on classical radiation damping, solving Maxwell's equations for the classical electromagnetic field along with the Heisenberg equation for a fictitious two level atom and a zero-spin one-electron atom, predicting radiative corrections to the lifetimes, line shapes, exponential decay and Lamb shifts. McClelland and Kelly (1985) took a more direct approach for the sodium atom, solving the optical Bloch equations for the elements of the density matrix. They reduced the number of coupled differential equations from 400, for the 20-state sodium problem, to 38 by making several approximations. The sodium optical pumping problem has since been solved using a full QED model by Farrell *et. al.* (1988). They later formulated this work in terms of experimental observables (Farrell *et. al.* 1991) and for the general case of elliptically polarised light (Varcoe *et. al.* 1999). It was shown that the optical pumping coefficients K and K' could be measured directly in a superelastic electron scattering arrangement, in terms of the polarisation of the decay fluorescence, by:

$$K = P_L \qquad \text{(eq. 4.4a)}$$

$$K' = P_C \qquad \text{(eq. 4.4b),}$$

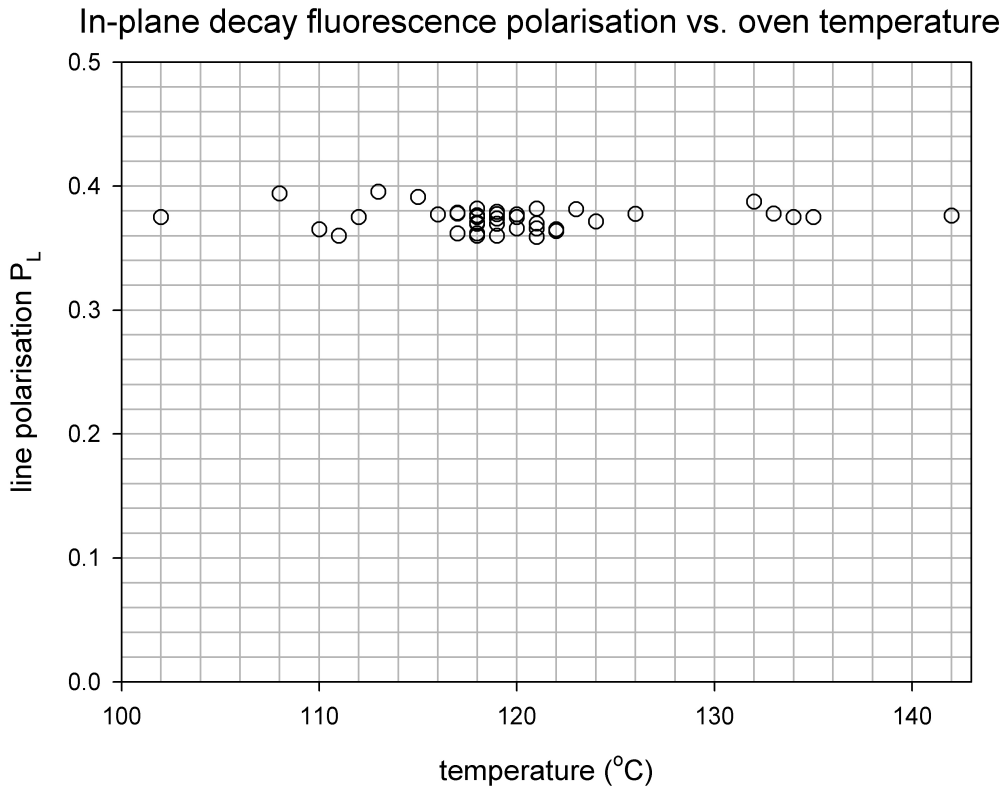

Figure 4.3: Decay fluorescence polarisation measured over a wide range of caesium oven temperatures, illustrating the stability of the optical pumping parameters for the atomic densities required for the present project. Atomic densities at the interaction region range from approximately 2×10^{9} *to* $1\times10^{10}\,cm^{-3}$ *across the entire indicated temperature scale (see also figure 3.4).*

where P_L is the linear polarisation of the decay fluorescence measured in the scattering plane, normal to the scattered electron direction, and P_C is the degree of circular polarisation measured normal to the scattering plane.

4.3 Optical Pumping Coefficients

In a superelastic electron scattering experiment the scattering rate is measured as a function of the laser polarisation, which in turn determines the quantum state of the target atoms. Unfortunately, in practice it is not possible to prepare perfectly polarised laser light and in general the polarisation must be considered to have some

degree of ellipticity. Thus the relative hyperfine sub-level populations for the target will reflect the specific conditions of the experiment. In correcting the equivalent Stokes parameters so that they allow for these optical pumping conditions, the optical pumping coefficients K and K' can be employed, where:

$$\overline{P_1} = \frac{1}{K} P_1$$
$$\overline{P_2} = \frac{1}{K} P_2 \qquad \text{(eq. 2.19).}$$
$$\overline{P_3} = \frac{1}{K'} P_3$$

Here P_i are the Stokes parameters measured directly from the scattering rates (equation 2.18) and $\overline{P_i}$ are the so-called reduced Stokes parameters (see also chapter 2). The optical pumping coefficients incorporate all aspects of the target state relevant to the collision dynamics and can take on values between 0 and 1, where 1 indicates complete pumping into the excited hyperfine state. They have been calculated for other alkalis (e.g. Farrell *et. al.* 1991, Hall *et. al.* 1996) and can be measured directly from the polarisation of the decay fluorescence. Throughout the present project, the optical pumping coefficients have been measured directly using the method of Scholten *et. al.* (1993): namely, a telephoto lens was installed outside the chamber in order to magnify an image of the interaction region, viewed within the scattering plane through a vacuum window which was perpendicular to the superelastic scattered electron momentum (chapter 3). This image was passed through a linear polariser, aligned either parallel ($\parallel$) or perpendicular ($\perp$) to the scattering plane, onto a photodiode detector, whose signal (F) was amplified and recorded. The measured line polarisation:

$$P_L = \frac{F_{\parallel} - F_{\perp}}{F_{\parallel} + F_{\perp}} \qquad \text{(eq. 4.2)}$$

yields information on a wide range of experimental parameters, including laser polarisation, intensity, frequency detuning and linewidth, the atomic beam density and divergence, and the laser-atom interaction times. The circular pumping coefficient, P_C, is the degree of circular polarisation of the target's decay fluorescence measured normal to the scattering plane, on the axis of the pump laser. Such measurements have been performed experimentally (for example see Scholten *et. al.* (1993) and Hanne *et. al.* (1993)), however the associated uncertainty in the measured data is usually large. In the past, it has been shown that P_C is practically independent of experimental conditions with the exception of very weak laser intensities (Farrell *et. al.* 1991). Within the present project, various attempts to deliberately misalign and shield the fluorescence detector from the laser did not result in P_C being significantly less than unity. Consider the allowed values of $\overline{P}_3$, combined with eq. 2.6:

$$\overline{P}_3 = \frac{P_3}{K'} \leq -1 \qquad \text{(eq. 4.3),}$$

and the data of figure 6.3 and table 6.3, which gives a maximum measured value of $\overline{P}_3 = -0.9016 \pm 0.0190$, at 60^o scattering angle and 15eV superelastic energy. Additionally, the measured values of $\overline{P}_3$ at 10eV superelastic energy, from figure 6.1 and table 6.1, yield:

$$\overline{P}_3 = \frac{P_3}{K'} \leq 1.0415 \pm 0.2189 \qquad \text{(eq. 4.3).}$$

This implies that $K' \geq 1.0415 \pm 0.2189$ and $K' \geq 0.9016 \pm 0.0190$ for these two energies, which in turn indicates that the coefficient P_C is indeed very close to unity.

Thus, throughout the superelastic scattering experiments reported in this thesis it is assumed that $P_C = 1$, and therefore $K' = 1$.

5 The Caesium Electron Scattering Experiments

5.0 Introduction

This chapter discusses the method by which the spin-averaged Stokes parameters for caesium were measured using the superelastic electron scattering technique. The experimental geometries are described and the measurement and analysis procedure is outlined. Finally the inherent statistical and systematic uncertainties are considered, with particular focus on their influence and limitations on the measured data.

5.1 Experimental Geometry

The reduced Stokes parameters $\overline{P}_1$, $\overline{P}_2$ and $\overline{P}_3$ were measured in a series of superelastic electron scattering experiments performed at a number of different electron energies and over a wide range of scattering angles. The geometry for the experiments was chosen so that all of the Stokes parameters could be determined without changing the path of the laser beam. The incident laser beam was normal to the scattering plane, which was defined by the electron gun and detector axes. The electron gun and detector were each mounted on separate independent rotating turntables which were coaxial with the laser beam (see figures 3.1, 3.2). An optical guide above the top window of the scattering chamber allowed the laser alignment to be checked when necessary without opening the chamber. The electron gun and spectrometer were aligned by using a removable guide to position each respective aperture at corresponding radial and vertical positions with respect to the chamber axis and the turntables. This alignment, essentially defining the scattering plane, was checked each time the apparatus was prepared for an experimental run. The

alignment procedure resulted in the laser being normal to the scattering plane, within an estimated uncertainty of $\pm 0.5^{\circ}$. This uncertainty was assumed to be negligible, particularly following a full treatment to correct for the effects of the finite angular resolution and interaction volume of the experiment (see section 5.4.2).

The experimental geometry shown in figures 5.1 and 5.2 enabled the electron detector to be fixed at up to four different positions: 0°, 45°, 90° and 135°. This not only allowed for a wide range of scattering angles to be accessed, but also permitted the experimental results to be examined for consistency and reproducibility. Separate measurements for positive and negative scattering angles, or for the same scattering angle with different analyser position, could be compared in order to determine the influence of external static fields or irregularities in the laser polarisation.

5.2 Experimental Procedure

The reproducibility of the experimental data depended strongly on the energy of the electron beam (see figure 5.3) and the correct polarisation of the laser radiation. The electron beam energy was thus calibrated before and after each experimental run using the procedure described in section 3.3.5, to ensure that the electron gun final cathode potential was set to within $\pm 0.1\,\mathrm{eV}$ of the intended incident electron energy. The degree of laser polarisation for each polarimeter arrangement (see figure 3.14) was measured above the upper window of the scattering chamber, before each experiment, using an analyser and photodiode detector. The primary purpose of this routine check was to ensure that the performance of the polarimeter did not become

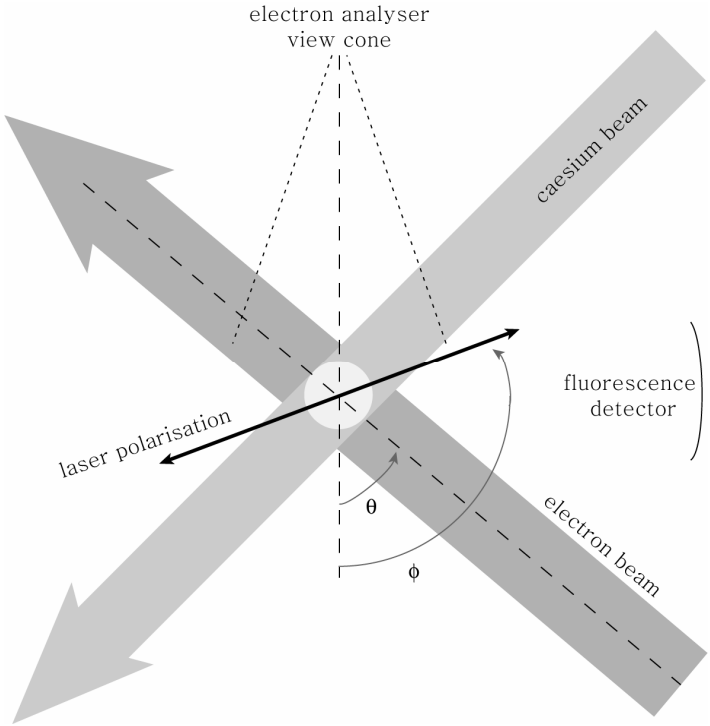

Figure 5.1: Experimental geometry (not to scale).

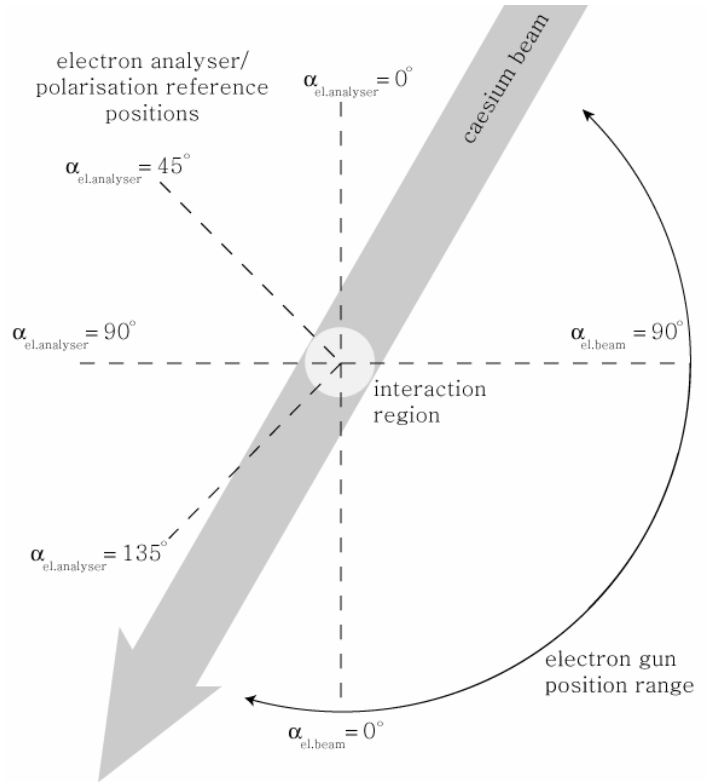

Figure 5.2: Electron gun and analyser angular positions (not to scale).

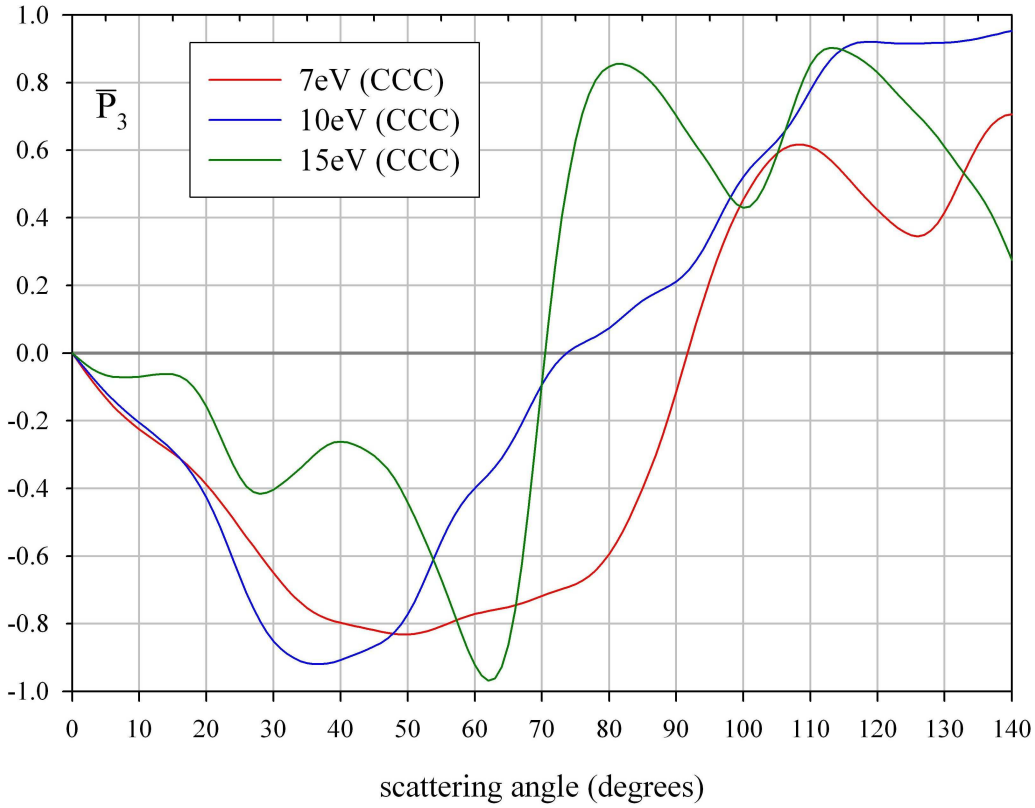

Figure 5.3: CCC calculations (Bray, 2006) for the reduced Stokes parameter $\overline{P}_3$ as a function of scattering angle for superelastic electron energies of 7eV, 10eV and 15eV. Features of particular interest are the zero crossing point and each extrema, all of which are strongly dependent on the electron energy.

influenced by minor drifts in laboratory temperature, and also to correct for any casual misalignment. Typical polarisation data from these measurements was provided in chapter 3.

The Stokes parameters were measured in the same run for each individual scattering angle. The scattering angle was set manually by rotating the electron gun turntable, while the data acquisition, laser beam shutter and polarimeter were computer-controlled. The decay fluorescence line polarisation (P_L), indicating the degree of orientation of the caesium target due to optical pumping, was recorded for $\phi = 0^\circ$

linear polarisation before and after each set of measurements. This procedure was then repeated for each scattering angle.

A typical single-angle experiment consisted of measuring the superelastic electron scattering rate over 10 seconds for seven intervals: six corresponding to each of the laser polarisation states and a final interval which was an elastic-only background count with the laser field removed by the beam shutter. The measured superelastic signal, *I*, was the difference between the total measured count rate, *S*, and the background count rate with the laser off, *B*:

$$I = S - B \qquad \text{(eq. 5.1).}$$

This process was repeated for a number of cycles dictated by the magnitude of the superelastic scattering rate and background count rate. Typical signal to background ratios ranged from 20:1 to around 3:1, depending on electron energy and scattering angle. As an example, a typical run could be for 10 cycles and each of the final number of superelastic counts over the entire 10 cycles, for a given laser polarisation, is substituted into the formula of eq. 2.18 in order to obtain the appropriate Stokes parameters P_1, P_2 and P_3. Total data acquisition times for a single angular set of measurements ranged from 20 minutes to 9 hours. Therefore this approach of measuring the entire set of polarisation-dependent scattering rates at short intervals in repetition was crucial in order to obtain the complete set of Stokes parameters in the same run, without the influence of any time-dependent drift in the experimental conditions.

After collecting scattering data in the form of the Stokes parameters P_1, P_2 and P_3,

corrections were made for the optical pumping conditions through the parameters K and K' (see section 4.3), yielding the reduced Stokes parameters $\overline{P_1}$, $\overline{P_2}$ and $\overline{P_3}$:

$$\overline{P_1} = \frac{1}{K}\frac{I(0^\circ) - I(90^\circ)}{I(0^\circ) + I(90^\circ)}$$

$$\overline{P_2} = \frac{1}{K}\frac{I(45^\circ) - I(135^\circ)}{I(45^\circ) + I(135^\circ)} \qquad \text{(eq. 5.2).}$$

$$\overline{P_3} = \frac{1}{K'}\frac{I(RHC) - I(LHC)}{I(RHC) + I(LHC)}$$

Usually several measurements were performed for any particular scattering angle, using rotated and/or reflected geometries to determine the possible influence of static charge build-up on the interior chamber surfaces and, in particular, to check for the influence of the unavoidable ellipticity of the laser polarisation (see section 5.4.3).

The final step in the experimental determination of the reduced Stokes parameters was to combine the separate measurements, with rotated and reflected scattering geometries, at each angle using the weighted mean formula of Taylor (1982):

$$\overline{P} = \frac{\sum_{n=1}^{N} w_n \overline{P}_n}{\sum_{n=1}^{N} w_n} \qquad \text{(eq. 5.3),}$$

where $\overline{P}$ is the weighted mean of each of the *n* individual measured values $\overline{P}_n$, weighted by the factor $w_n = (\delta\overline{P}_n)^{-2}$, where $(\delta\overline{P}_n)$ is the relative uncertainty for that measurement. This formula enables a mean value to be extracted from all of the available data, weighted accordingly so that the final data takes into account the uncertainty of each of the individual measurements.

5.3 Statistical Uncertainties

In any experiment, a counting measurement is subject to some statistical uncertainty. If the events that are being counted are independent of the number of events occurring immediately beforehand, and do not occur simultaneously, then the process can be accurately modeled by Poisson statistics (Snyder 1975). Following Barford (1967), the number of events governed by Poisson statistics, when counted repeatedly over the equal time intervals, will yield a number of counts that varies by no more than $\sqrt{N}$, where N is the mean number of events that can occur within that interval. The statistical error in a count of N events within some time interval is therefore given by:

$$\delta N = \sqrt{N} \qquad \text{(eq. 5.4)}$$

and consequently the relative statistical error is:

$$\frac{\delta N}{N} = \frac{1}{\sqrt{N}} \qquad \text{(eq. 5.5).}$$

This result reveals that the relative error in any counting measurement decreases with the number of counts. For the case of the superelastic experiment, the relative statistical error decreases with increasing scattered electron count rate and acquisition duration. From equations 5.1 and 5.2, it is clear that each of the Stokes parameters depend on both the superelastic signal and the background signal, each measured at separate time intervals. A full treatment of the propagation of errors in this case is given in the Appendix, leading to the statistical uncertainty for each of the Stokes parameters as functions of the measured observables:

$$\delta\overline{P_1} = \frac{1}{K^2}\left(\left|K\frac{4}{(I_0 + I_{90})}\sqrt{I_{90}^2(S_0 + B_0) + I_0^2(S_{90} + B_{90})}\right| + \left|P_1\delta K\right|\right) \qquad \text{(eq. 5.6)}$$

$$\delta\overline{P}_2 = \frac{1}{K^2}\left(\left|K\frac{4}{(I_{45}+I_{135})}\sqrt{I_{135}^2(S_{45}+B_{45})+I_{45}^2(S_{135}+B_{135})}\right|+\left|P_2\delta K\right|\right) \quad \text{(eq. 5.7)}$$

$$\delta\overline{P}_3 = \left|\frac{4}{(I_{RHC}+I_{LHC})}\right|\sqrt{I_{LHC}^2(S_{RHC}+B_{RHC})+I_{RHC}^2(S_{LHC}+B_{LHC})} \quad \text{(eq. 5.8).}$$

Finally, the statistical uncertainty in the coherence parameter can be represented in terms of the parameters $\overline{P}_1$, $\overline{P}_2$ and $\overline{P}_3$, and their corresponding uncertainties:

$$\delta P^+ = \frac{1}{P^+}\left(\left|\overline{P}_1\delta\overline{P}_1\right|+\left|\overline{P}_2\delta\overline{P}_2\right|+\left|\overline{P}_3\delta\overline{P}_3\right|\right) \quad \text{(eq. 5.9).}$$

5.4 Systematic Uncertainties

5.4.1 Scattering Angle

The scattering angle was defined throughout the experiments as the angle between the scattered electron trajectory and the incident electron beam. It is the independent variable in the present study, therefore it is crucial that this angle is measured carefully and correctly. Standard procedures were employed to align the electron gun and analyser turntables by optical and mechanical means, however this approach was not satisfactory to determine the true zero scattering angle. This follows as the electron trajectories may each depend on localised magnetic and electrostatic fields which must be investigated with each experimental run. Initial measurements for small positive and negative scattering angles enabled the P_1 maximum at $\theta = 0°$ to be used as a calibration feature. Additionally, the symmetry in each of the Stokes parameters could be employed at larger scattering angles to check for any possible offset in the scattering angle. Finally, the rotated scattering geometries discussed in section 5.1 enabled another check for alignment and consistency in the scattering angle measurements. Throughout the present study, the

total systematic uncertainty in the scattering angle measurements was found to be less than $\pm 0.2°$.

5.4.2 Angular Resolution

An ideal electron scattering experiment consists of an electron analyser with energy and angular resolutions which are very small, and a target which can be regarded as a point-like scattering centre. In a real experiment, however, one cannot assume the angular resolution to be negligible and therefore the angular-dependent parameter should be treated as an average over a finite range of scattering angles. This finite angular range is determined chiefly by the angular field of view of the electron spectrometer, the angular divergence of the electron beam and the volume of the scattering target. One aim of the caesium superelastic experiments was to reduce this angular range to a minimum, within practical limits, and also to accurately measure this total angular resolution quantitatively, at each electron energy, for subsequent data analysis.

Theoretical calculations are generally performed for the ideal conditions: the target interaction volume is considered to be a single point and the angular resolution is negligible. There have been several studies on the influence of the angular resolution and finite scattering volume on angular dependent parameters, most notably by Mitroy *et. al.* (1987), Zetner *et. al.* (1990) and Becker *et. al.* (1992). Zetner *et. al.* (1990) explored the effects of a finite scattering volume on superelastic electron scattering experiments with barium, in an approach which included a treatment for both the unresolved in-plane scattering angles and the out-of-plane effects due to the finite scattering volume. They observed that the influence of the finite scattering volume on the electron scattering experiment was most pronounced at small

scattering angles, confirming the earlier observations of Register *et. al.* (1983). The experimentalist can attempt to predict the influence of the scattering geometry by the use of a convolution transform, which folds the theoretical scattering parameter with the differential cross section and a function that reflects the angular uncertainties particular to the apparatus. Consider a scattering parameter P, ideally being a function of scattering angle θ, measured by an electron scattering experiment. In practice, instead of being able to measure $P(\theta)$ directly, we measure $\langle P \rangle$ which is the parameter P, weighted by the differential cross section σ and averaged over the range of uncertainty of the scattering angle, both in and out of the scattering plane. This uncertainty in scattering angle is determined by both the experimental arrangement and the characteristics of the instruments themselves. The convolution formula of Mitroy *et. al.* (1987) can be used to represent the output of such a measurement:

$$\langle P \rangle = \frac{\langle I(\alpha_1) \rangle - \langle I(\alpha_2) \rangle}{\langle I(\alpha_1) \rangle + \langle I(\alpha_2) \rangle} = \frac{(P\sigma) * H}{\sigma * H} \qquad \text{(eq. 5.10),}$$

where σ represents the differential cross section and H represents the uncertainty in scattering angle due to all experimental and instrumental conditions. In many cases, particularly in the superelastic experiment (see for example Sang *et. al.* 1994, Stockman *et. al.* 1999 and Karaganov *et. al.* 1999), the interaction region can be contained to a small volume and thus the out-of-plane scattering can be considered to be much less significant than the in-plane effects. In this case, H can be substituted by the instrument function, $h(\theta)$, of the apparatus. This reduces the convolution formula to (Mitroy *et. al.* 1987):

$$\langle P \rangle = \frac{(P\sigma) * h}{\sigma * h} = \frac{\int_{-\infty}^{\infty} d\phi\, h(\theta - \phi) P(\phi) \sigma(\phi)}{\int_{-\infty}^{\infty} d\phi\, h(\theta - \phi) \sigma(\phi)} \qquad \text{(eq. 5.11).}$$

When solving equation 5.11 numerically, the limits of integration in the above formula can be truncated to a range which sufficiently represents the width of the instrument function:

$$\langle P(\theta)\rangle = \frac{\int_{\theta-\delta\theta}^{\theta+\delta\theta} d\phi\, h(\theta-\phi)P(\phi)\sigma(\phi)}{\int_{\theta-\delta\theta}^{\theta+\delta\theta} d\phi\, h(\theta-\phi)\sigma(\phi)} \qquad \text{(eq. 5.12).}$$

The instrument function is itself a convolution of a number of angular dependent 3-dimensional functions that characterise the experimental geometry. Specifically for the case of the present superelastic experiments, the instrument function is:

$$h(\theta) = h_{el.beam} * h_{el.analyser} * h_{scatt.vol.} \qquad \text{(eq. 5.13),}$$

where each of the functions on the right-hand side of eq. 5.13 represent the angular characteristics of the apparatus (see figure 5.4). $h_{el.beam}$ is a function characterising the electron beam angular divergence, weighted by the spatial intensity profile, $h_{el.analyser}$ is a function characterising the angular resolution of the electron analyser, weighted by the spatial response, and $h_{scatt.vol.}$ characterises the spatial distribution of the excited caesium atoms. In practice, each of these functions cannot be known exactly, but must be approximated in some way. Conventionally, these functions can be accurately modeled by Gaussian functions, in which case the FWHM of the total instrument function can be derived from eq. 5.13, for the present experiments:

$$\Delta\alpha_{all} = \sqrt{\Delta\alpha_{el.beam}^2 + \Delta\alpha_{el.analyser}^2 + \Delta\alpha_{scatt.vol.}^2} \qquad \text{(eq. 5.14)}$$

from the respective FWHM of each individual Gaussian function. The divergence of the electron beam, $\Delta\alpha_{el.beam}$, was estimated by direct measurement throughout the superelastic experiments, whereas the angular resolution of the electron analyser, $\Delta\alpha_{el.analyser}$, and the scattering volume, $\Delta\alpha_{scatt.vol.}$, were estimated from the

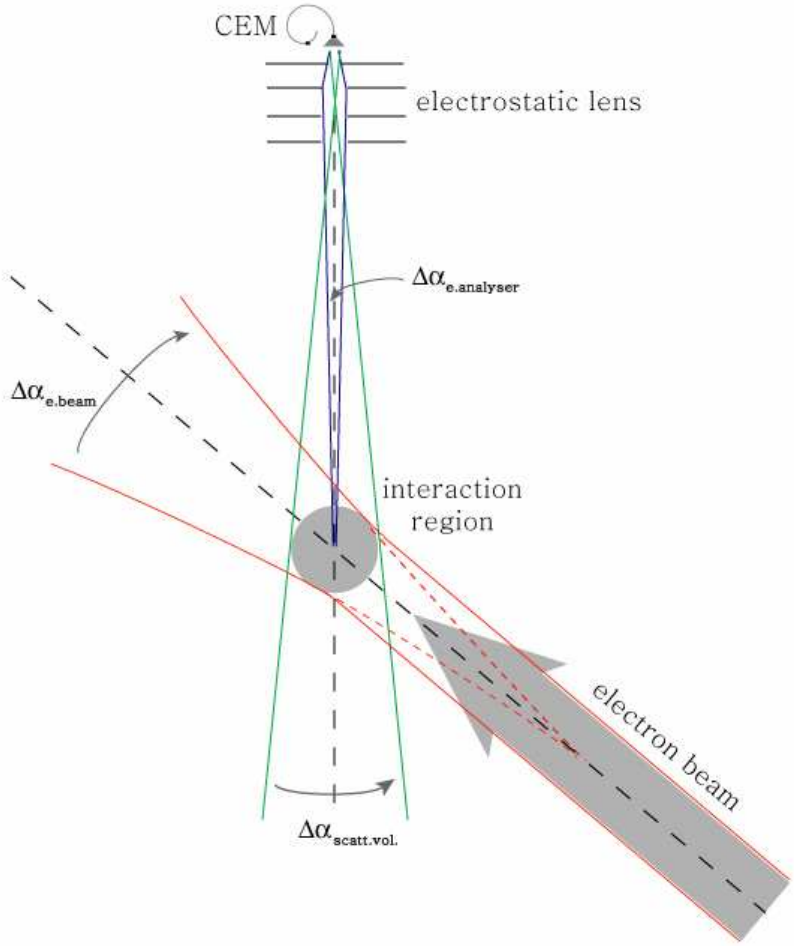

Figure 5.4: The electron beam divergence, electron analyser angular resolution and the angular uncertainty due to the finite scattering volume, all of particular interest when determining the instrument function of the apparatus (diagram not to scale).

experimental conditions and geometry (see chapter 3 and section 5.1). Typical values of $\Delta\alpha_{all}$ were found to be:

$$\Delta\alpha_{all} \approx \sqrt{(4.5^\circ)^2 + (4.4^\circ)^2 + (2.6^\circ)^2} = 6.8^\circ \qquad \text{(eq. 5.15)}$$

for 5.5eV incident electron energy, and

$$\Delta\alpha_{all} \approx \sqrt{(2.5^\circ)^2 + (4.4^\circ)^2 + (2.6^\circ)^2} = 5.7^\circ \qquad \text{(eq. 5.16)}$$

for 13.5eV incident electron energy.

The results reported in chapter 6 of this thesis are compared with relevant theoretical predictions which have been folded numerically using the convolution formula of eq. 5.12 in each case. The integration was performed numerically using a modified Simpson method, and the appropriate Gaussian instrument function of FWHM due to eq. 5.14. For illustration, a typical plot of the reduced Stokes parameter $\overline{P}_2$, calculated using the CCC theory of Bray (2006), before and after folding is displayed in figure 5.5.

5.4.3 Laser Polarisation

Even with the angular resolution and extinction limitations of the polarising optics carefully considered and minimised (see section 3.4), an additional small elliptical element was introduced with the laser beam passing through the glass window of the scattering chamber. While the chamber windows were initially isotropic, they were inevitably subjected to strain when the scattering chamber was evacuated. This strain resulted in the windows being slightly birefringent when the experiment was under operating conditions (Born and Wolf 1980). It was difficult to measure the extent of this effect directly, due to the fact that the analysing photodetector was by necessity located outside the chamber, which introduced a second window in the beam path. Scholten *et. al.* (1999) investigated the influence of imperfect laser polarisation on the scattering density matrix and the reduced Stokes parameters. It was shown that some generalised reduced Stokes parameters, $\overline{P}_i'$, measured with imperfect laser polarisation, can be represented by the equations:

$$\overline{P}_1' = \frac{\kappa_{11}\overline{P}_1 + \kappa_{12}\overline{P}_2}{1 + \kappa_{13}\overline{P}_3} \qquad \text{(eq. 5.17a)}$$

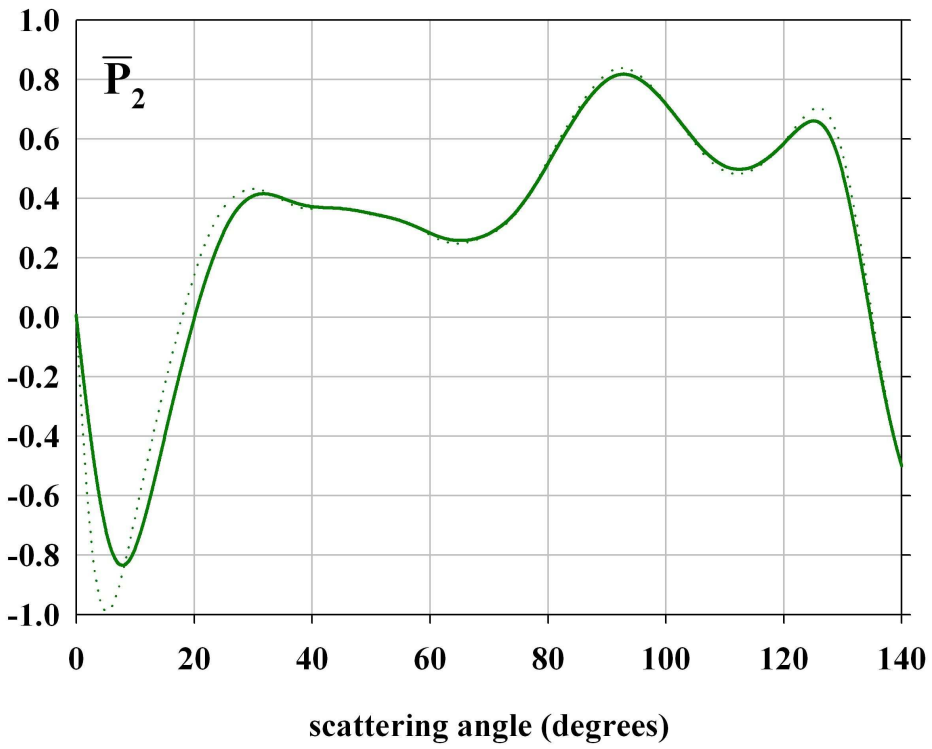

Figure 5.5: Convergent Close Coupling calculation (Bray 2006) of the reduced Stokes parameter $\overline{P}_2$ *(dashed line), alongside the same calculation folded (solid line) with the differential cross section and a Gaussian instrumental function of* 6.8° *(FWHM). The superelastic electron energy is 7eV.*

$$\overline{P}_2' = \frac{\kappa_{22}\overline{P}_2 + \kappa_{21}\overline{P}_1}{1+\kappa_{23}\overline{P}_3} \qquad \text{(eq. 5.17b)}$$

$$\overline{P}_3' = \frac{\kappa_{33}\overline{P}_3 + \kappa_{32}\overline{P}_2}{1+\kappa_{31}\overline{P}_1} \qquad \text{(eq. 5.17c),}$$

where the coefficients $\kappa_{12,13}$ are the effect of $\overline{P}_2$ and $\overline{P}_3$ influencing the $\overline{P}_1'$ measurements, $\kappa_{21,23}$ are the effect of $\overline{P}_1$ and $\overline{P}_3$ influencing the $\overline{P}_2'$ measurements, and similarly $\kappa_{31,32}$ are the effect of $\overline{P}_1$ and $\overline{P}_2$ influencing the $\overline{P}_3'$ measurements. For small imperfections in polarisation, we can expect all of the coefficients to be small, except for $\kappa_{11,22,33}$, which will be close unity. For practical applications, it was found that for small polarisation ellipticity, the circular polarisation contribution

to $\overline{P}_1$ and $\overline{P}_2$ due to $\overline{P}_3$ could be determined by measuring $\overline{P}_1$ on both sides of zero scattering angle (*i.e.* for both positive and negative angles). For all of the measurements reported here this contribution was found to be small when compared with the statistical uncertainty, even for angles where $\overline{P}_3$ was large and therefore the circular polarisation contribution was at a maximum. This process was, however, an essential check to ensure that the polarisation ellipticity was reduced to the experimental limit. It is also worth noting that the contributions due to $\overline{P}_1$ and $\overline{P}_2$ on $\overline{P}_3$ were found to be negligible by the equivalent process, so it was assumed that similarly the contributions due to $\overline{P}_1$ and $\overline{P}_2$ on each other were also negligible. Some characteristic $\overline{P}_1$ values from measurements either side of zero scattering angle are shown in figure 5.6. In practice, the final value of $\overline{P}_1$ was taken as the average of the positive and negative angle values for each scattering angle θ, using the procedure outlined in section 5.2.

5.4.4 Electron Energy

The energy of the incident electron beam was maintained by a potential on the oxide cathode of the electron gun. This was provided by a 0.01V-precision programmable power supply, as described in section 3.3.1. Due to the variable contact potential of the BaO cathode (see section 3.3.5), the beam energy was calibrated against the b-feature in the excitation function of metastable neon at regular intervals. This procedure was undertaken both before and after each experimental run in order to maintain the desired incident electron energy. The thermal energy spread in the incident electron beam was approximately 0.3eV (Simpson 1967), while the

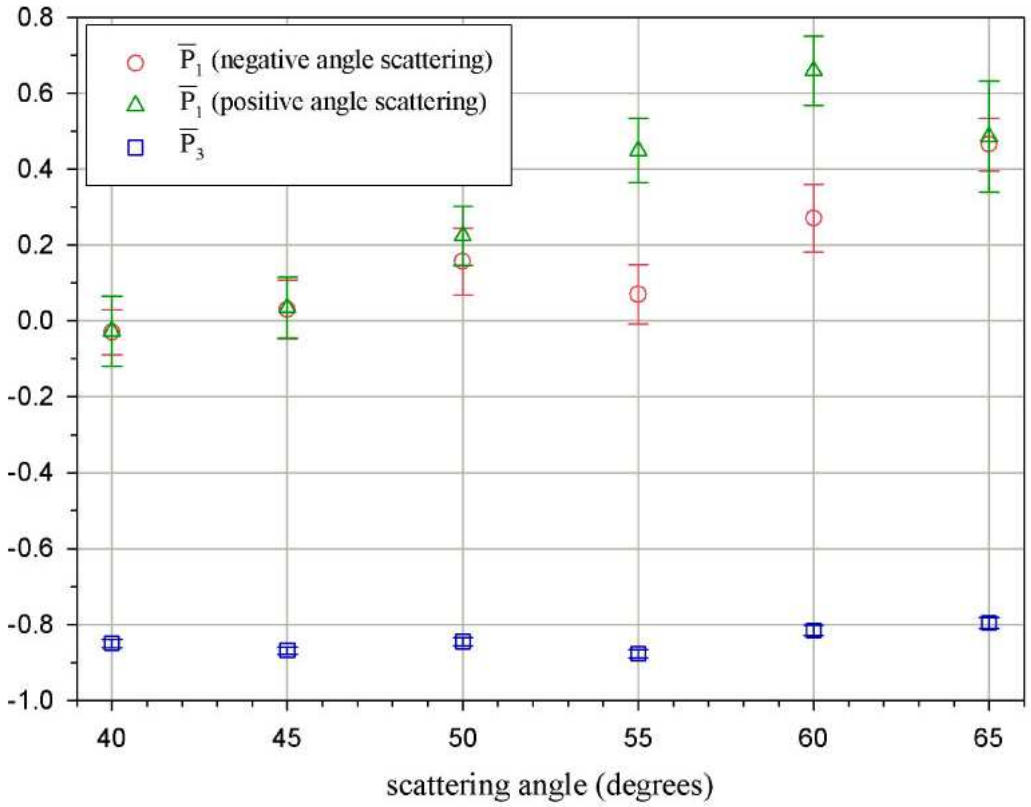

Figure 5.6: Comparison between measured values of $\overline{P}_1$ with positive and negative angle geometries, for scattering angles near 50°, where $\overline{P}_3$ (and therefore its contribution to $\overline{P}_1$ due to any small elliptical component to the laser polarisation) is large. The superelastic electron energy is 7eV.

estimated uncertainty in the beam energy, due to the energy calibration method, was a much smaller $\pm 0.06\,\text{eV}$. Therefore the total error in the electron energy, due to each contributing factor, was estimated to be less than $\pm 0.3\,\text{eV}$.

5.5 Summary of Experimental Uncertainties

The total uncertainty in each of the reduced Stokes parameters measured by the superelastic electron scattering technique reported here consists of a significant statistical error, determined directly during data acquisition and analysis of each set of measured data, and a systematic error which is thought to have a much less significant influence on the final results. For example, the influence on the

experimentally determined reduced Stokes parameters, due to the uncertainty in electron energy, depends strongly on the scattering angle and in general cannot be known exactly. However, the maximum uncertainty was estimated to be $\left|\Delta\overline{P}_3\right| \leq 0.054$ (see figure 5.3) and less than this value for $\Delta\overline{P}_1$ and $\Delta\overline{P}_2$, which generally each have a somewhat smaller dependence on electron energy. The influence of the uncertainty in laser polarisation on the final data has been eliminated where possible, by the averaging technique described in sections 5.4.3 and 5.2 and elsewhere can be assumed to be small. It is worth noting that this assumption is particularly valid for the parameter $\overline{P}_3$, which has a much lower sensitivity to laser polarisation ellipticity. Combined with its lower sensitivity to angular resolution effects due to its smooth structure, particularly at small scattering angles compared to $\overline{P}_1$ and $\overline{P}_2$, $\overline{P}_3$ is perhaps the most favourable parameter to measure from an experimentalists point of view. Due to the difficulty in accurately reporting systematic uncertainties which have such strong and varied dependence on the scattering angle, a great effort has been made to reduce these systematic effects and, once these were minimal, to include only the statistical uncertainties in the final results. This is the case for all of the experimental results reported in chapter 6. The uncertainty in scattering angle is estimated to be known to better than $\pm 0.2°$ in all cases, and has not been included in the plotted results in the interests of clarity for the reader.

6 Experimental Results and Discussions

6.0 Introduction

In this chapter the current experimental results are presented for a complete set of spin-averaged Stokes parameters and the coherence parameter P^+, for the $6^2P_{3/2}$ state in caesium, after electron impact de-excitation for superelastic energies of 7eV and 15eV. Additionally, the spin-averaged Stokes parameter $\overline{P_3}$ is presented for the 10eV superelastic energy and compared with the results of a previous experimental study. The data presented in each case span a range of scattering angles from 5 degrees to 135 degrees. For each energy, the experimental data are compared with the predictions of a CCC theory and an RMPS theory, which were described previously in chapter 2. Predictions from an RDW theory, kindly provided by Prof. Bob McEachran, are also presented for the 10eV superelastic electron energy. The data from both the CCC and RMPS theories are unpublished and have been generously supplied by Prof. Igor Bray and Prof. Klaus Bartschat.

6.1 Results

The experimentally determined spin-averaged Stokes parameters and the coherence parameter P^+, for electron-caesium superelastic scattering, are presented in figures 6.1 to 6.3 and also in numerical form (tables 6.1 to 6.3) at the end of the chapter. The error bars represent plus and minus one standard deviation, calculated using the procedure outlined in chapter 5. The theoretical data presented in figures 6.1-6.3 are folded with the relevant differential cross-section, as calculated by the respective theories, and the instrumental function reflecting the experimental angular resolution at the relevant energy, as described in chapter 5. It should be noted that, in general,

for the reduced Stokes parameters the folding procedure has negligible influence for all but the very forward angles, where the differential cross section is largest. The coherence parameter is predicted by theory (Bray 2006, Bartschat 2006) to be close to unity $P^+ \approx 1$, for all scattering angles, if finite experimental angular resolution effects are neglected. It is important to note here that the inclusion of finite angular resolution produces some structure in the coherence parameter. This structure should not be misinterpreted as being due to exchange scattering effects (see section 2.4). The data contained in the reduced Stokes parameters can also be reinterpreted in terms of the alignment and orientation parameters through equations 2.12, whereby the parameters $\overline{P}_1$ and $\overline{P}_2$ contain the information on the linear polarisation, $\overline{P}_L$, and the alignment angle, γ, of the P-state electron charge cloud and $\overline{P}_3$ is related directly to the angular momentum transfer perpendicular to the scattering plane, $L_\perp$:

$$L_\perp = -\overline{P}_3 \qquad \text{eq. 6.1.}$$

10eV / 8.5eV

A series of preliminary superelastic electron scattering experiments were performed at 10eV superelastic electron energy (8.5eV incident electron energy) by Karaganov *et. al.*, prior to the current work reported here. This early study, while originally planned to be a preliminary survey, was found to be completely reproducible. The present results that confirm the earlier values of the reduced Stokes parameter $\overline{P}_3$, are displayed in figure 6.1 and table 6.1. Note that the complete set of spin-averaged reduced Stokes parameters for the preliminary survey, at 10eV electron scattering from caesium can be found in Karaganov *et. al.* (2002). In this case, each of the RDW (McEachran 2001), RMPS (Bartschat 2001) and CCC (Bray 2001) theories

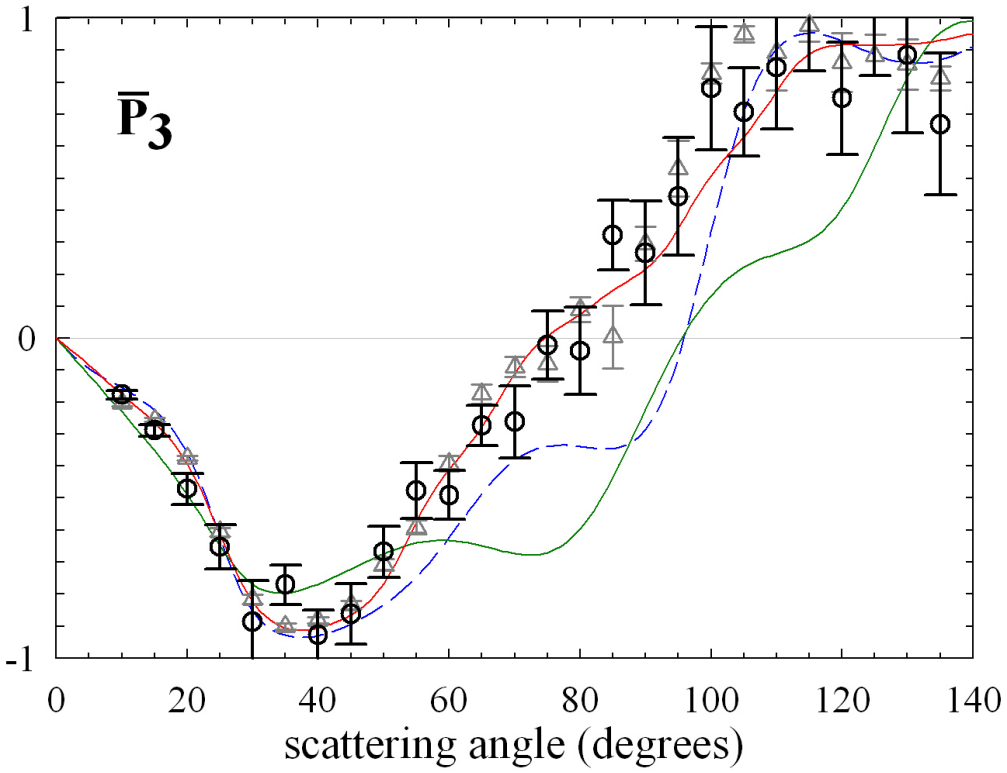

Figure 6.1: Present reduced Stokes parameter $\overline{P}_3$, measured using the superelastic technique (o), alongside the earlier experimental data of Karaganov et. al. (2001) (△). Also shown is an RMPS calculation of Bartschat (2001) (----), a CCC calculation of Bray (2001) (——) and a RDW calculation of McEachran et. al.*(2001) (——). The scattered and incident electron energies are 10 eV and 8.5 eV, respectively.*

accurately predict the scattering parameter for forward angles ($\theta \leq 30°$), however the CCC is clearly superior at describing the behaviour for $50° \leq \theta \leq 100°$. For scattering angles greater than $100°$, both the CCC and the RMPS provide an adequate description of the scattering process.

7eV / 5.5eV

The current experimental results for 7eV superelastic electron energy are shown in figure 6.2 and table 6.2. In their graphical form, they are compared with a 24-state RMPS calculation from Bartschat (2006) and a fully-converged CCC calculation from Bray (2006). The data span a wide range of scattering angles from 10 degrees through to 135 degrees. For the reduced Stokes parameters $\overline{P}_1$ and $\overline{P}_2$, there is a

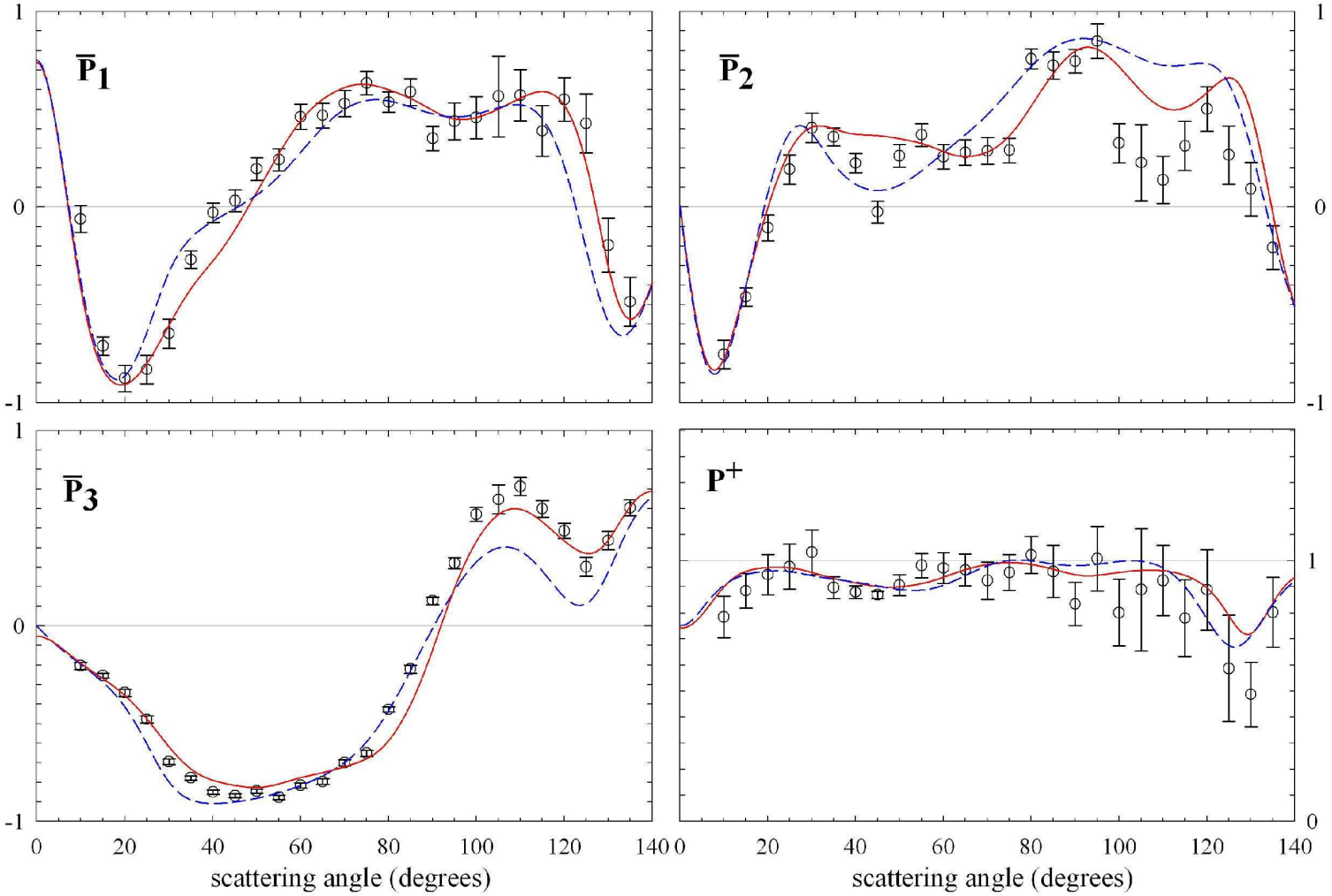

Figure 6.2: Present reduced Stokes parameters $\overline{P}_1$, $\overline{P}_2$, $\overline{P}_3$ and coherence parameter P^+, measured using the superelastic technique (∘). Also shown is an RMPS calculation (Bartschat 2006) (- - - -) and a CCC calculation (Bray 2006) (——). The scattered and incident electron energies are 7 eV and 5.5 eV, respectively.

suggestion of some significant disagreement between the experimental results and the predictions of both theories, particularly at intermediate angles around 40 degrees and for backward scattering angles in the case of $\overline{P}_2$. The apparent failure of the CCC, to accurately describe each of the minima in $\overline{P}_2$ at 40 degrees and 110 degrees, is likely to be due to an incomplete description of the target core potential (Bray 2006). In contrast, the parameter $\overline{P}_3$ shows a quite remarkable level of agreement with both the RMPS and the CCC theories. The experimental data in this case can be perceived to marginally favour the CCC, with the exception of the zero crossing point at approximately 87 degrees, where the RMPS predictions are in closer accord with the measured data. There also appears to be a minimal disagreement between experiment and both theoretical calculations in the coherence parameter, although it is barely significant to within the experimental uncertainties.

15eV / 13.5eV

The results from the experimental study at 15eV superelastic electron energy are summarised in figure 6.3 and table 6.3. In this case, the lower magnitude of the differential cross section at backward angles limited the angular range to forward and intermediate angle scattering: $5° \leq \theta \leq 90°$. Once again, the predictions of fully-converged CCC (Bray 2005) and 24-state RMPS (Bartschat 2005) calculations are compared with the experimental results in figure 6.3. The agreement between the CCC calculation and the experimental data is excellent for each of the reduced Stokes parameters and the coherence parameter. Unfortunately the experimental results did not reach beyond the 90 degree scattering angle, where the only observable difference in structure exists between the RMPS and CCC theories for the parameter $\overline{P}_2$. The plot of $\overline{P}_1$ confirms that the RMPS calculation has perhaps

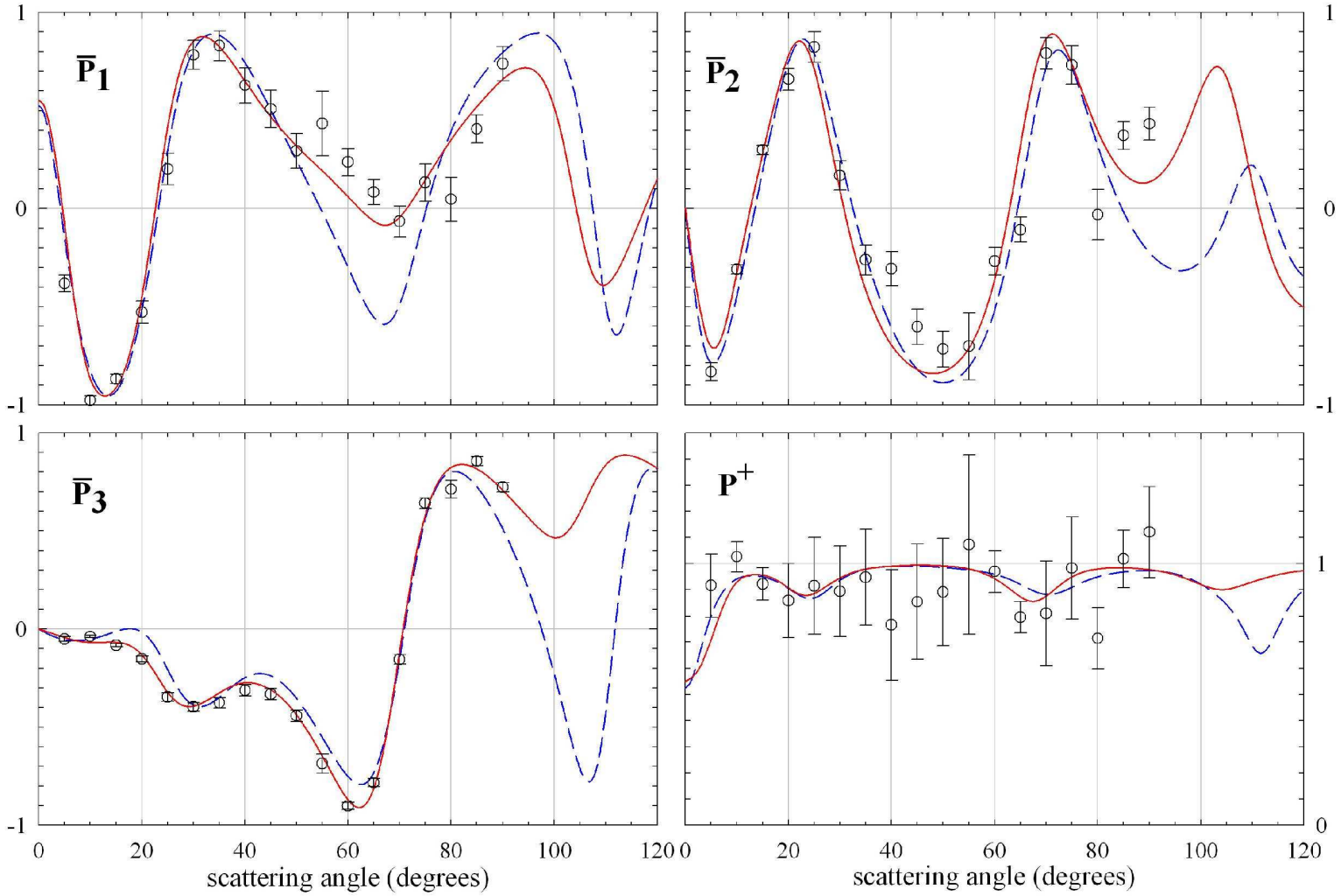

Figure 6.3: Present reduced Stokes parameters $\overline{P_1}$, $\overline{P_2}$, $\overline{P_3}$ and coherence parameter P^+, measured using the superelastic technique (∘). Also shown is an RMPS calculation (Bartschat 2006) (----) and a CCC calculation (Bray 2006)(——). The scattered and incident electron energies are 15 eV and 13.5 eV, respectively.

not achieved complete convergence with a 24-state computation, while the CCC has accurately predicted the shallow minimum at 70 degrees. The experimentally determined $\overline{P}_3$ parameter is found to be in almost perfect agreement with the CCC calculation across the entire angular range.

Scattering Angle (degrees)	$\overline{P}_3$	$\left\vert \delta\overline{P}_3 \right\vert$
10	-0.1775	0.0127
15	-0.2883	0.0183
20	-0.4719	0.0479
25	-0.6530	0.0686
30	-0.8861	0.1285
35	-0.7709	0.0624
40	-0.9268	0.0764
45	-0.8621	0.0946
50	-0.6679	0.0803
55	-0.4769	0.0869
60	-0.4912	0.0760
65	-0.2733	0.0626
70	-0.2623	0.1119
75	-0.0219	0.1075
80	-0.0400	0.1371
85	0.3220	0.1097
90	0.2658	0.1618
95	0.4426	0.1841
100	0.7808	0.1926
105	0.7071	0.1379
110	0.8462	0.1926
115	1.0128	0.1764
120	0.7500	0.1747
125	1.0415	0.2189
130	0.8846	0.2420
135	0.6692	0.2221

Table 6.1: Present reduced Stokes parameter $\overline{P}_3$ and its experimental uncertainty, as measured using the superelastic technique. The scattered and incident electron energies are 10 eV and 8.5 eV, respectively.

Scattering Angle (degrees)	$\overline{P}_1$	$\lvert\delta\overline{P}_1\rvert$	$\overline{P}_2$	$\lvert\delta\overline{P}_2\rvert$	$\overline{P}_3$	$\lvert\delta\overline{P}_3\rvert$	P^+	$\lvert\delta P^+\rvert$
10	-0.0612	0.0687	-0.7548	0.0721	-0.2045	0.0188	0.7845	0.0797
15	-0.7114	0.0468	-0.4607	0.0470	-0.2538	0.0127	0.8847	0.0658
20	-0.8765	0.0679	-0.1060	0.0667	-0.3423	0.0175	0.9469	0.0767
25	-0.8306	0.0728	0.1926	0.0751	-0.4780	0.0183	0.9775	0.0856
30	-0.6472	0.0744	0.4047	0.0749	-0.6949	0.0151	1.0323	0.0862
35	-0.2697	0.0452	0.3583	0.0456	-0.7770	0.0111	0.8971	0.0414
40	-0.0293	0.0499	0.2237	0.0493	-0.8500	0.0107	0.8794	0.0246
45	0.0322	0.0559	-0.0253	0.0558	-0.8685	0.0097	0.8695	0.0134
50	0.1949	0.0583	0.2617	0.0590	-0.8453	0.0107	0.9061	0.0396
55	0.2421	0.0573	0.3688	0.0585	-0.8770	0.0110	0.9817	0.0460
60	0.4611	0.0638	0.2569	0.0635	-0.8159	0.0138	0.9717	0.0586
65	0.4687	0.0627	0.2789	0.0645	-0.7957	0.0143	0.9647	0.0609
70	0.5296	0.0663	0.2867	0.0690	-0.6998	0.0159	0.9233	0.0715
75	0.6345	0.0603	0.2896	0.0626	-0.6522	0.0148	0.9549	0.0691
80	0.5370	0.0515	0.7580	0.0517	-0.4268	0.0142	1.0223	0.0713
85	0.5879	0.0684	0.7242	0.0700	-0.2210	0.0202	0.9586	0.0995
90	0.3512	0.0621	0.7455	0.0603	0.1291	0.0191	0.8341	0.0830
95	0.4383	0.0942	0.8485	0.0878	0.3209	0.0279	1.0075	0.1238
100	0.4576	0.1081	0.3265	0.1005	0.5707	0.0360	0.8011	0.1283
105	0.5661	0.2069	0.2266	0.1945	0.6467	0.0734	0.8889	0.2348
110	0.5717	0.1310	0.1380	0.1212	0.7135	0.0450	0.9246	0.1338
115	0.3889	0.1300	0.3127	0.1259	0.5991	0.0424	0.7797	0.1479
120	0.5494	0.1111	0.5019	0.1135	0.4858	0.0389	0.8887	0.1540
125	0.4279	0.1525	0.2658	0.1498	0.3019	0.0490	0.5873	0.2041
130	-0.1953	0.1389	0.0916	0.1359	0.4368	0.0471	0.4872	0.1235
135	-0.4847	0.1245	-0.2077	0.1117	0.6045	0.0407	0.8022	0.1348

Table 6.2: Present reduced Stokes parameters $\overline{P}_1$, $\overline{P}_2$, $\overline{P}_3$, the coherence parameter P^+ and their corresponding experimental uncertainties, as measured using the superelastic technique. The scattered and incident electron energies are 7 eV and 5.5 eV, respectively.

Scattering Angle (degrees)	$\overline{P}_1$	$\lvert\delta\overline{P}_1\rvert$	$\overline{P}_2$	$\lvert\delta\overline{P}_2\rvert$	$\overline{P}_3$	$\lvert\delta\overline{P}_3\rvert$	P^+	$\lvert\delta P^+\rvert$
5	-0.3811	0.0442	-0.8315	0.0452	-0.0505	0.0123	0.9161	0.1198
10	-0.9779	0.0227	-0.3096	0.0222	-0.0381	0.0058	1.0264	0.0580
15	-0.8684	0.0242	0.2991	0.0242	-0.0826	0.0068	0.9222	0.0618
20	-0.5281	0.0563	0.6598	0.0555	-0.1524	0.0153	0.8588	0.1410
25	0.2014	0.0789	0.8225	0.0774	-0.3466	0.0219	0.9150	0.1851
30	0.7835	0.0745	0.1686	0.0739	-0.3966	0.0217	0.8942	0.1730
35	0.8296	0.0772	-0.2607	0.0761	-0.3759	0.0257	0.9473	0.1833
40	0.6281	0.0895	-0.3068	0.0879	-0.3113	0.0289	0.7652	0.2111
45	0.5076	0.0948	-0.6022	0.0911	-0.3314	0.0295	0.8545	0.2209
50	0.2946	0.0882	-0.7159	0.0907	-0.4422	0.0297	0.8916	0.2047
55	0.4344	0.1650	-0.7014	0.1705	-0.6856	0.0503	1.0727	0.3433
60	0.2367	0.0701	-0.2684	0.0701	-0.9016	0.0190	0.9700	0.0803
65	0.0838	0.0640	-0.1076	0.0640	-0.7834	0.0211	0.7952	0.0602
70	-0.0653	0.0787	0.7918	0.0792	-0.1554	0.0238	0.8096	0.1997
75	0.1330	0.0949	0.7322	0.0978	0.6420	0.0260	0.9828	0.1946
80	0.0479	0.1110	-0.0306	0.1287	0.7123	0.0449	0.7146	0.1173
85	0.4061	0.0716	0.3725	0.0710	0.8557	0.0222	1.0178	0.1100
90	0.7387	0.0881	0.4324	0.0835	0.7234	0.0233	1.1207	0.1746

Table 6.3: Present reduced Stokes parameters $\overline{P}_1$, $\overline{P}_2$, $\overline{P}_3$, the coherence parameter P^+ and their corresponding experimental uncertainties, as measured using the superelastic technique. The scattered and incident electron energies are 15 eV and 13.5 eV, respectively.

7 Conclusions

The work presented in this thesis details the first superelastic electron scattering experiments with caesium. Four spin-averaged parameters have been determined in order to describe the electron-caesium collision process. Specifically, the complete set of spin-averaged reduced Stokes parameters ($\overline{P}_1$, $\overline{P}_2$ and $\overline{P}_3$) and the coherence parameter (P^+) have been measured for superelastic electron energies of 7eV and 15eV, for a wide range of scattering angles, and compared with the predictions of two of the most sophisticated theories that are currently available, namely the Convergent Close Coupling theory (Bray and Stelbovics 1992, Bray 2006) and the R-matrix with pseudostates theory (Bartschat and Fang 2000, Bartschat 2006). Additionally, the reduced Stokes parameter $\overline{P}_3$ is reported for 10eV superelastic electron energy, confirming preliminary results due to Karaganov *et. al.* (2002). The CCC predictions of Bray (2001, 2005, 2006) are in very good quantitative agreement across the entire range of electron energies and scattering angles, while the RMPS predictions of Bartschat (2001, 2005, 2006) generally compare favourably, but fail in determining the complete structure of the reduced Stokes parameters. In most cases this lack of definitive agreement is probably due to its higher demand for computational resources leading to slower, and in some cases incomplete, convergence.

This experimental study on caesium is the fifth in a series of superelastic electron scattering experiments conducted at Flinders University. The previous experimental studies have included sodium (Scholten 1989), calcium (Law 1994), lithium (Karaganov 1997) and potassium (Stockman 2000). The present work thus

concludes a set of superelastic electron scattering experiments spanning most of the alkali-metal group. Note that the missing element, rubidium, has been studied at Griffith University by Hall *et. al.* (2004). These elements are of particular interest as scattering targets because they consist of a single outer-shell electron orbiting an "inert" core, thereby simplifying the theoretical treatment to that of a hydrogen-like target. This therefore allows a deeper understanding of the scattering process to be achieved, without complications due to interactions between many electrons within a target. One of the primary motivations for undertaking the present project is that caesium, being the heaviest of the alkalis, is considered to be useful in determining the role of relativistic effects in electron-atom collisions. The non-relativistic CCC theory had previously been found to yield very accurate predictions for the other alkali targets for a wide range of energies (Scholten 1993, Karaganov 1997, Stockman 2000, Hall 2004), but this was not expected to persist for caesium. However, during the course of this project, it has been found that the CCC theory can in fact well describe the behaviour of the reduced Stokes parameters for caesium over a wide range of scattering angles at low to intermediate energies. Hence it is clear that any relativistic effects in electron caesium scattering must be very small, for the kinematical regime investigated in this thesis. Consequently, a study of these relativistic effects will require spin-polarised electron and caesium beams.

Appendix

Formulae for the reduced Stokes parameters and the propagation of errors.

The data collected throughout the superelastic experiments are derived from the measured electron count rates at the chosen scattering angle and laser polarisation. The statistical uncertainty associated with such a counting measurement N is equal to one standard deviation (see section 5.3):

$$\delta N = \sqrt{N} \qquad \text{(eq. A1)}$$

Specifically, each of the Stokes parameters P_1, P_2 and P_3 and the reduced Stokes parameters $\overline{P_1}$, $\overline{P_2}$ and $\overline{P_3}$, for a given scattering angle, are derived from the measured quantities B (the electron count rate with the no laser excitation) and S (the electron count rate with the atomic target pumped). The measured quantities can be labelled with the subscripts S_0, S_{90}, S_{45}, S_{135}, S_{LHC}, S_{RHC} to denote the count rate for each of the relevant laser polarisations employed to achieve a full set of reduced Stokes parameters.

Following Taylor (1982), the propagation of errors can be written:

$$\delta F = \sum_i \left| \frac{\delta F}{\delta x_i} \delta x_i \right| \qquad \text{(eq. A2)}$$

and

$$\delta F = \sqrt{\sum_i \left(\frac{\delta F}{\delta x_i} \delta x_i \right)^2} \qquad \text{(eq. A3),}$$

where F is a function of the measured quantities x_i, with measurement errors δx_i. Equation A3 is only applicable for quantities x_i which are statistically independent, otherwise equation A2 should be used.

In chapter 2, the reduced Stokes parameters were defined (see eqs. 2.18 and 2.19):

$$\begin{aligned} \overline{P_1} &= \frac{1}{K}\frac{I_0 - I_{90}}{I_0 + I_{90}} \\ \overline{P_2} &= \frac{1}{K}\frac{I_{45} - I_{135}}{I_{45} + I_{135}} \\ \overline{P_3} &= \frac{1}{K'}\frac{I_{RHC} - I_{LHC}}{I_{RHC} + I_{LHC}} \end{aligned} \qquad \text{(eq. A4)}$$

where the subscript denotes the polarisation of the laser and K and K' are optical pumping parameters. The electron scattering count rate I is found from the measured superelastic signal S minus the background B. Thus the propagation of errors for $\overline{P_1}$, using eq. A2, is:

$$\delta\overline{P_1} = \frac{1}{K^2}\left(\left|K\delta P_1\right| + \left|P_1\delta K\right|\right) \qquad \text{(eq. A5),}$$

where the Stokes parameter, in terms of the experimentally measured quantities, is:

$$P_1 = \frac{(S_0 - B_0) - (S_{90} - B_{90})}{(S_0 - B_0) + (S_{90} - B_{90})} \qquad \text{(eq. A6)}$$

and has a statistical uncertainty (from eq. A3):

$$\delta P_1 = \frac{4}{(I_0 + I_{90})}\sqrt{I_{90}^2(S_0 + B_0) + I_0^2(S_{90} + B_{90})} \qquad \text{(eq. A7),}$$

and therefore following eq. A5,

$$\delta\overline{P_1} = \frac{1}{K^2}\left(\left|K\frac{4}{(I_0 + I_{90})}\sqrt{I_{90}^2(S_0 + B_0) + I_0^2(S_{90} + B_{90})}\right| + \left|P_1\delta K\right|\right) \qquad \text{(eq. A8).}$$

Similarly for $\overline{P_2}$ and $\overline{P_3}$:

$$\delta P_2 = \frac{4}{(I_{45} + I_{135})} \sqrt{I_{135}^2 (S_{45} + B_{45}) + I_{45}^2 (S_{135} + B_{135})} \qquad \text{(eq. A9)}$$

$$\delta P_3 = \frac{4}{(I_{RHC} + I_{LHC})} \sqrt{I_{LHC}^2 (S_{RHC} + B_{RHC}) + I_{RHC}^2 (S_{LHC} + B_{LHC})} \qquad \text{(eq. A10)}$$

and

$$\delta \overline{P}_2 = \frac{1}{K^2} \left(\left| K \frac{4}{(I_{45} + I_{135})} \sqrt{I_{135}^2 (S_{45} + B_{45}) + I_{45}^2 (S_{135} + B_{135})} \right| + \left| P_2 \delta K \right| \right) \qquad \text{(eq. A11)}$$

$$\delta \overline{P}_3 = \frac{1}{K'^2} \left(\left| K' \frac{4}{(I_{RHC} + I_{LHC})} \sqrt{I_{LHC}^2 (S_{RHC} + B_{RHC}) + I_{RHC}^2 (S_{LHC} + B_{LHC})} \right| + \left| P_3 \delta K' \right| \right)$$

(eq. A12).

Thus the statistical uncertainty in each of the reduced Stokes parameters depends on the count rate of the measured superelastic and background signals and on the optical pumping parameters. Note that the contribution by δK or $\delta K'$ to the error should be considered a systematic rather than statistical uncertainty. In the case of the present study, it was assumed that K' and $\delta K'$ were unity and zero, respectively. In this case the error in $\overline{P}_3$ is:

$$\delta \overline{P}_3 = \left| \frac{4}{(I_{RHC} + I_{LHC})} \right| \sqrt{I_{LHC}^2 (S_{RHC} + B_{RHC}) + I_{RHC}^2 (S_{LHC} + B_{LHC})} \qquad \text{(eq. A13).}$$

The coherence parameter, P^+, was defined in section 2.4:

$$P^+ = \sqrt{\overline{P}_1^2 + \overline{P}_2^2 + \overline{P}_3^2} \qquad \text{(eq. A14).}$$

The statistical uncertainty in the coherence parameter depends on each of the parameters $\overline{P}_1$, $\overline{P}_2$ and $\overline{P}_3$, and their corresponding uncertainties, which should not be considered as statistically independent. Therefore, from eq. A2, the statistical uncertainty in the coherence parameter is:

$$\delta P^+ = \frac{1}{P^+} \left(\left| \overline{P}_1 \delta \overline{P}_1 \right| + \left| \overline{P}_2 \delta \overline{P}_2 \right| + \left| \overline{P}_3 \delta \overline{P}_3 \right| \right) \qquad \text{(eq. A15).}$$

References

Ackerhalt, JR, and Eberly, JH (1974). Phys. Rev. D **10 (10)** 3350.

Andersen, N, Gallagher, JW and Hertel, IV (1985). *Proceedings of the 14th International Conference on the Physics of Electronic Collisions*, Palo Alto (Amsterdam; Holland).

Andersen, N, Gallagher, JW and Hertel, IV (1988). Phys. Rep. **165**, 1-188.

Andersen, N, Bartschat, K, Broad, JT, and Hertel, IV (1997). Phys. Rep. **279**, 251.

Andersen, N, and Bartschat, K (2001). *Polarization, Alignment and Orientation in Atomic Collisions*. Springer-Verlag (New York).

Barford, NC (1967). *Experimental Measurements: Precision, Error and Truth.* Addison Wesley Pub. Co. (London).

Bartschat, K (1993). J. Phys. B. **26** 3595-3609.

Bartschat, K (2001) *private communication.*

Bartschat, K (2005) *private communication.*

Bartschat, K (2006) *private communication.*

Bartschat, K, and Fang, Y (2000). Phys. Rev. A. **62** 052719.

Baum, G, Forster, S, Pavlovic, N, and Roth, B (2004). Phys. Rev. A **70** 012707.

Becker, K, Crowe, A, and McConkey, JW (1992). J. Phys. B. **25** 3885-3913.

Bederson, B (1969a). Comments At. Mol. Phys. **1** 41.

Bederson, B (1969a). Comments At. Mol. Phys. **1** 65.

Blum, K (1981). *Density Matrix Theory and Applications*, Plenum Press (New York).

Born, M and Wolf, E (1980). *Principles of Optics: electromagnetic theory of propagation, interference and diffraction of light.* 6th ed., Pergamon Press (Oxford; New York).

Bray, I, (1996). Aust. J. Phys. **49** 201-217.

Bray, I, (2001) *private communication.*

Bray, I, (2005) *private communication.*

Bray, I, (2006) *private communication.*

Bray, I, Fursa, DV and McCarthy, IE, (1994). Phys. Rev. A **49 (4)** 2667-2674.

Bray, I, and Stelbovics, AT (1992). Phys. Rev. A **46 (11)** 6995-7011.

Bray, I, and Stelbovics, AT (1995). Comp. Phys. Comm. **85** 1-17.

Brotherton, TD, Cole, ON and Davis, RE (1962). *Properties and Handling Procedures for Rubidium and Cesium Metals.* Trans. Metallurgical Soc. AIME, **224** 287.

Buckman, SJ, Hammond, P, King, GC and Read, FH (1983). J. Phys. B, **28**, 1889.

Burke, PG, Hibbert, A, and Robb, WD (1971). J. Phys. B **4** 153-161.

Burke, PG, and Mitchell, JFB (1974). J. Phys. B. **7** 214.

Burke, PG, and Scott, MP, (1996). *The R-Matrix Method*, in Bartschat, K (ed.), *Computational Atomic Physics: Electron and Positron Collisions with Atoms and Ions*, Springer (Berlin).

Burke, PG, and Smith, K (1962). Rev. Mod. Phys. **34 (3)** 458-502.

Chen, ST, and Gallagher, AC (1978). Phys. Rev. A **17 (2)** 551-560.

Demtroder, W (1996). *Laser spectroscopy : basic concepts and instrumentation 2nd ed.*, Springer (Berlin; New York).

Dixon, AJ, Hood, ST and Weigold, E (1978). Phys. Rev. Lett. **40 (19)** 1262-1266.

Eminyan, M, MacAdam, KB, Slevin, J and Kleinpoppen, H (1973). Phys. Rev. Lett. **31 (9)** 576-579.

Farrell, PM, MacGillivray, WR, and Standage, MC (1988). Phys. Rev. A **37 (11)** 4240.

Farrell, PM, MacGillivray, WR, and Standage, MC (1991). Phys. Rev. A **44 (3)** 1828.

Franzen, W and Emslie, AG (1957). Phys. Rev. **108 (6)**, 1453.

Gerginov, V, Tanner, CE, Diddams, S, Bartels, A and Hollberg, L (2004). Phys. Rev. A **70 (4)**, 2505.

Gerritsen, HJ and Nienhuis, G (1975). App Phys Lett, **26 (6)**, 347.

Haas, GA (1967). *Electron Sources, Thermionic*, in *Methods of Experimental Physics Vol.4, Atomic and Electron Physics, Part A, Atomic Sources and Detectors*, Academic Press (New York; London).

Hall, BV, Sang, RT, Shurgalin, M, Farrell, PM, MacGillivray, WR and Standage, MC (1996). Can. J. Phys. **74** 977-983.

Hall, BV, Shen, Y, Murray, AJ, Standage, MC, MacGillivray, WR, and Bray, I (2004). J. Phys. B **37** 1113-1124.

Hanne, GF, McClelland, JJ, Scholten, RE and Celotta, RJ (1993). J. Phys. B **26** L753-L758.

Hansen, W (1984). J. Phys. B **17** 4833.

Harting, E and Read, FH, with contributions by Brunt, JNH (1976). *Electrostatic Lenses*, Elsevier Scientific Pub. Co. (Amsterdam; New York).

Hertel, IV and Stoll, W (1974). J. Phys. B **7 (5)** 583-592.

Jacka, M, Kelly, J, Lohmann, B and Buckman, SJ (1995). J. Phys. B **28** L361-366.

Johnson, PV, and Zetner, PW (2005). J. Phys. B. **38 (15)** 2793-2810.

Karaganov, V (1997). *Electron Scattering from Optically Pumped Lithium*, PhD Thesis (Flinders University).

Karaganov, V, Bray, I, Teubner, PJO and Farrell, PM (1996). Phys. Rev. A **54** R9.

Karaganov, V, Bray, I, and Teubner, PJO (1999). Phys. Rev. A **59 (6)** 4407.

Karaganov, V, Teubner, PJO, and Brunger, MJ, (2002), in *Correlations, Polarization and Ionization in Atomic Systems*, AIP Conference Proceedings **604**, American Institute of Physics (Melville).

Karule, E, (1972). J. Phys. B **5** 2051.

Kessler J (1985). *Polarized Electrons*, 2nd ed, Springer (Berlin; New York).

Law, MR (1994). *Electron Scattering from Calcium*, PhD Thesis (Flinders University).

Law, MR and Teubner, PJO (1995). J. Phys. B **28 (11)** 2257-2267.

Lew, H (1967). *Secondary Emission by Metastable Atoms*, in *Methods of Experimental Physics Vol.4, Atomic and Electron Physics, Part A, Atomic Sources and Detectors*, Academic Press (New York; London).

Lucas, CB (1973). Vacuum **23 (11)**, 395.

Lukomski, M, MacAskill, JA, Seccombe, DP, McGrath, C, Sutton, S, Teewuen, J, Kedzierski, W, Reddish, TJ, McConkey, JW and van der Wijngaarden, WA (2005). J. Phys. B **38** 3535-3545.

MacAskill, JA, Kedzierski, W, McConkey, JW, Domyslawska, J and Bray, I, (2002). J. Electron Spectrosc. Relat. Phenom. **123** 173-184.

Macek, J and Hertel, IV (1974). J. Phys. B **7 (16)** 2173-2188.

Macek, J. and Jaecks, DH (1971). Phys. Rev. A **4 (6)** 2288-2300.

MacGillivray, WR, and Standage, MC (1991). Comments At. Mol. Phys. **26 (4)** 179-201.

Mantell, CL (1958). *Engineering Materials Handbook*, MacGraw-Hill (New York).

McClelland, JJ, and Kelly, MH (1985). Phys. Rev. A **31 (6)** 3704.

McEachran, RP, (2001) *private communication.*

Mitroy, J, McCarthy, IE, Stelbovics, AT, (1987). J. Phys. B. **20** 4827-4850.

Murray, AJ, and Cvejanovic, D (2003). J. Phys. B. **36 (24)** 4889-4910.

Nesmeyanov, AN (1963). *Vapour pressure of the chemical elements*, Elsevier (Amsterdam).

Perel'man, FM (1965), *Rubidium and Caesium*, Pergamon Press (Oxford).

Register, DF, Trajmar, S, Csanak, G, Jensen, SW, Fineman, MA and Poe, RT (1983). Phys. Rev. A **28 (1)** 151-159.

Riley, JL (1984). *Coherence in Inelastic Electron Scattering from Sodium*, PhD Thesis (Flinders University).

Riley, JL, Teubner, PJO, Brunger, MJ, (1985). Phys. Rev. A **31 (3)** 1959-1961.

Sang, RT, Farrell, PM, Madison, DH, MacGillivray, WR, and Standage, MC (1994). J. Phys. B **27** 1187-1208.

Scholten, RE, Shen, GF, and Teubner, PJO (1993). J. Phys. B **26** 987-1004.

Scholten, RE (1989) *Electron Scattering from Optically Pumped Sodium*, PhD Thesis (Flinders University).

Scholten, RE, Karaganov, V, Teubner, PJO and Farrell, PM (1999). Phys. Rev. A **60 (1)** 330-336.

Scott, NS, and Burke, PG, (1980). J. Phys. B. **13**, 4299-4314.

Shurcliff, WA, (1962). *Polarized Light; production and use*. Harvard University Press (Cambridge).

Simpson, JA (1967). Characteristics of Electron Sources, in *Methods of Experimental Physics Vol.4, Atomic and Electron Physics, Part A, Atomic Sources and Detectors*, Academic Press (New York; London).

Snyder, DL, (1975). *Random Point Processes*. Wiley (New York).

Sobel'man, I I (1972). *Introduction to the Theory of Atomic Spectra*, Pergamon Press (New York).

Stockman, KA (2000). *Laser Assisted Electron Scattering from Potassium*, PhD Thesis (Flinders University).

Stockman, KA, Karaganov, V, Bray, I, and Teubner, PJO (2001). J. Phys. B **34** 1105-1114.

Stockman, KA, Karaganov, V, Bray, I, and Teubner, PJO (1999). J. Phys. B **32** 3003-3013.

Stokes, GG (1852). Trans. Cambridge Phil. Soc., Vol. IX, 399.

Taylor, JR (1982). *An Introduction to Error Analysis: the Study of Uncertainties in Physical Measurements*, Oxford University Press (Oxford).

Teubner, PJO and Scholten, RE (1992). J. Phys. B **25** L301.

Varcoe, BTH, Sang, RT, MacGillivray, WR and Standage, MC 1999. J. Modern Optics **46 (5)**, 787-800.

Walker, DW (1974). J. Phys. B **7** L489.

Weast, R (1981), *CRC Handbook of Chemistry and Physics 61st ed.*, CRC Press, Inc (Boca Raton, Florida).

Zeman, V, McEachran, RP, and Stauffer, AD (1993). Z. Phys. D **30** 145-148.

Zeman, V, McEachran, RP, and Stauffer, AD (1994). J. Phys. B **27** 3175-3188.

Zeman, V, McEachran, RP, and Stauffer, AD (1995). J. Phys. B **28** 3063-3077.

Zeman, V, McEachran, RP, and Stauffer, AD (1997). J. Phys. B **30** 3475-3490.

Zetner, PW, Trajmar, S and Csanak, G (1990). Phys. Rev. A **41 (11)** 5980-5999.